GFZ
Helmholtz-Zentrum
POTSDAM

HELMHOLTZ-ZENTRUM POTSDAM
DEUTSCHES
GEOFORSCHUNGSZENTRUM

Zhou, G. G. D., Lu, X., Xie, Y., Cui, K. F. E., Tang, H. (2022): Mechanisms of the Non-uniform Breach Morphology Evolution of Landslide Dams Composed of Unconsolidated Sediments During Overtopping Failure. - Journal of Geophysical Research: Earth Surface, 127, 10, e2022JF006664.

https://doi.org/10.1029/2022JF006664

Institional Repository GFZpublic: https://gfzpublic.gfz-potsdam.de/

Check for updates

ADVANCING EARTH AND SPACE SCIENCE

JGR Earth Surface

RESEARCH ARTICLE
10.1029/2022JF006664

Key Points:

- Erosion along dam surfaces varies non-uniformly in both vertical and lateral directions
- The non-uniform breach morphology evolution promotes a positive feedback between the breach flow velocity and dam surface gradients
- The gradual saturation of the breach flow with sediment influences the non-uniform breach morphology evolution of breaching landslide dams

Supporting Information:

Supporting Information may be found in the online version of this article.

Correspondence to:

X. Lu,
luxueqiang18@mails.ucas.ac.cn

Citation:

Zhou, G. G. D., Lu, X., Xie, Y., Cui, K. F. E., & Tang, H. (2022). Mechanisms of the non-uniform breach morphology evolution of landslide dams composed of unconsolidated sediments during overtopping failure. *Journal of Geophysical Research: Earth Surface*, *127*, e2022JF006664. https://doi.org/10.1029/2022JF006664

Received 3 MAR 2022
Accepted 14 SEP 2022

© 2022. American Geophysical Union. All Rights Reserved.

Mechanisms of the Non-Uniform Breach Morphology Evolution of Landslide Dams Composed of Unconsolidated Sediments During Overtopping Failure

Gordon G. D. Zhou[1,2,3], Xueqiang Lu[1,2], Yunxu Xie[1], Kahlil F. E. Cui[1], and Hui Tang[4]

[1]Key Laboratory of Mountain Hazards and Earth Surface Process, Institute of Mountain Hazards and Environment, Chinese Academy of Sciences, Chengdu, China, [2]University of Chinese Academy of Sciences, Beijing, China, [3]China-Pakistan Joint Research Center on Earth Sciences, CAS-HEC, Islamabad, Pakistan, [4]Section 4.7: Earth Surface Process Modelling, GFZ German Research Centre for Geosciences, Potsdam, Germany

Abstract Overtopping flows in landslide dams erode and entrain materials on the dam surface resulting in erosional features that undermine the dam stability and facilitate the subsequent outburst flooding. A comprehensive understanding of dam surface evolution is therefore crucial for flood risk assessment and hazard mitigation. In this research, we study the mechanisms that influence the non-uniform morphology evolution of landslide dam breaches (i.e., non-linear variation of the dam surface gradient) through experiments and numerical modeling. Analog landslide dam models, constructed using unconsolidated poorly sorted soils, are exposed to different inflow discharges. We find that although the breach discharge evolves more consistently with the erosion along the sidewalls than with bed erosion, it is the erosion along the bed that controls the change in dam surface profiles. Erosion rates, expressed as a function of the difference between the flow shear stress and the apparent erosion resistance, vary at different points along the dam surface due to localized erosional features induced by scouring. The apparent erosion resistance is found to increase linearly along the dam surface. Dam failure is numerically modeled using depth-averaged equations which assume that the complex evolution of the dam profiles is due to the coupled effects of erosion, entrainment, and channel bed collapse. Good agreement between the observed and modeled dam profiles further demonstrates that the gradual saturation of the breach flow with entrained sediment is responsible for the linear variation of the apparent erosion resistance, which in turn contributes to the formation of the surface scouring.

Plain Language Summary Landslides that occur near rivers may block the incoming water flow forming natural dams. Landslide dams fail when the impounded water breaches the top of the dam. As the breaching flow travels along the downstream surface of the dam, it erodes surface sediment. Experiments have shown that this erosion is not uniform and that it results in non-linear changes in the dam surface steepness. Accurate modeling of both the erosion and the evolution of the dam surface profile is important for the prediction and mitigation of outburst floods that threaten downstream establishments. In this work, we investigate the factors that shape landslide dam surfaces during dam breaches through experiments and numerical modeling. We used landslide dam models composed of unconsolidated sediments to better understand their failure process under different inflow conditions. A numerical dam failure model captures the observed complex erosion behaviors and replicates measured dam surface profiles. We then find that non-uniform erosion is related to the saturation of the outburst floods with sediment as it travels downstream. The saturation diminishes the flood's ability to erode and entrain more surface material. This numerical model may help enhance early warning strategies for landslide dam outburst flooding.

1. Introduction

Landslides such as debris slides, rock avalanches, etc. (Hungr et al., 2014), can result in the local blockage of river channels and the formation of landslide dams. The formation and failure of landslide dams are common geophysical and geomorphic processes in mountainous regions (Costa & Schuster, 1988; Ermini & Casagli, 2003; Korup, 2002; X. Fan et al., 2021). A recent survey of these events (L. M. Zhang et al., 2016) reported 1,267 landslide dams worldwide before 2010. Approximately 24% of these events formed between the years 2000 and 2010, including 257 dams triggered by the M_s 8.0 Wenchuan earthquake in China last 2008 (P. Cui et al., 2009). Landslide dams typically consist of unconsolidated, poorly sorted soils that are highly vulnerable to breaching

21699011, 2022, 10, Downloaded from https://agupubs.onlinelibrary.wiley.com/doi/10.1029/2022JF006664 by Helmholtz-Zentrum Potsdam GFZ, Wiley Online Library on [21/11/2022]. See the Terms and Conditions (https://onlinelibrary.wiley.com/terms-and-conditions) on Wiley Online Library for rules of use; OA articles are governed by the applicable Creative Commons License

(Davies et al., 2007). Outburst floods resulting from dam breaches are types of non-meteorological floods (O'Connor & Beebee, 2009) that pose serious threats to residents, their livelihoods, and local infrastructure downstream (Costa & Schuster, 1988; Larese et al., 2015; X. M. Fan et al., 2020). These floods are short-lived and are usually several orders of magnitude greater than the discharges of the receiving rivers (Cenderelli & Wohl, 2001; Cook et al., 2018). Such processes can dramatically change the landscapes along the river channels (Brunner et al., 2020; Lang et al., 2013) and are major drivers of geomorphic evolution in mountain areas (Cook et al., 2018).

Landslide dam breaching processes are controlled by complex mechanisms which involve overtopping, seepage, localized collapses, and slope failure (Costa & Schuster, 1988; Davies et al., 2007; Korup, 2002). The primary failure mechanism is often overtopping, accounting for more than 90% of reported cases, complemented by either seepage or slope failure (Korup, 2004; Peng & Zhang, 2012). After a landslide blocks a river channel, the upstream water level gradually rises due to continuous inflow. Overtopping occurs when the water level exceeds the height of the dam. Several works focusing on the overtopping process (Feliciano Cestero et al., 2015; Garcia-Castellanos & O'Connor, 2018; Walder et al., 2015) found that the discharge at the dam shoulder upstream Q_b is related to the outburst discharge Q_{out} downstream. The change of Q_{out} with time, known as outburst hydrographs, can be predicted if Q_b is well-known (Chang & Zhang, 2010; Coleman et al., 2002). Indeed, to understand the temporal evolution of hydrographs, previous studies have been dedicated to defining the evolution of Q_b in terms of the changes in the breach geometry (e.g., Davies et al., 2007; Hakimzadeh et al., 2014; Macchione & Rino, 2008; Walder & O'Connor, 1997) and hydraulic controls (e.g., Castro-Orgaz et al., 2022; Hager & Schwalt, 1994; Haun et al., 2011). Recently, G. G. D. Zhou et al. (2019) showed that the water flow at the dam shoulder initially appears to be sediment-free (i.e., clear water flow) but later evolves into turbulent sediment-laden flow (i.e., muddy water flow), or even debris flow, further downstream. This suggests that landslide dam failure is an erosion process along the flow direction and the sediment entrainment during the dam breach should also be considered in determining Q_{out}.

The breaching process is physically tied to the breach morphology evolution, especially along the direction of the breach flow. Figure 1a shows a schematic diagram of a landslide dam breach process adopted in recent literature (e.g., Argentin et al., 2021; Korup, 2005; X. Fan et al., 2021) in a coordinate system where x is along the flow direction, y is along the lateral direction, while z is normal to the river bed. In this illustration, Q_b is measured from the upstream dam shoulder (labeled section II) while Q_{out} is measured at the dam toe. Both measurement locations may be displaced as the overtopping flood deforms the dam through erosion. Erosion during dam breaching occurs along the lateral (y-axis) and vertical (normal to the bed) directions and is quantified by the sidewall erosion rate $E_w = dw_{bj}/dt$ (Figure 1b) and the bed erosion rate $E_b = dh_{sj}/dt$ (Figure 1c) respectively. Several previous works have proposed conceptual models defining the longitudinal (x-direction) evolution of the breach channel profile during different stages of a dam breach. Some of these breach models are summarized in Table 1. Earlier conceptual models proposed by Fread (1988) and Visser (1999) assume that the change of the dam surface, as it is eroded by the breach flow, is uniform (i.e., surface gradient is constant). Later models depict dam surface evolution as a step-wise process accounting for sharp inhomogeneities in the breach flow conditions at the dam crest and at the slope surface. The abovementioned models assume that these erosion mechanisms remain uniform with time until the impounded water or the dam is depleted. On the other hand, G. G. D. Zhou et al. (2019) showed that during breaching the dam surface morphology is highly "non-uniform" (i.e., dam surface gradient is not constant), characterized by the emergence of scour holes, which can be likened to the step-pools that develop when water flows over cohesive soils (Izumi & Parker, 2000; Parker & Izumi, 2000). They speculated that this non-uniform surface evolution might be due to localized variations of the apparent erosion resistance, but they were not able to provide a quantitative expression for this mechanism. In addition, the evolution of sidewall erosion is often assumed to be uniform or is completely ignored in dam breaching models, including those featured in Table 1. This is despite the fact that landslide dam sidewalls are often unstable due to their unconsolidated material composition, and E_w should vary along the dam surface in response to changes in hydrodynamic conditions (Davies et al., 2007; Korup & Tweed, 2007).

As the flood passes through the dam shoulder onto the downstream slope, the flow velocity may vary significantly due to sudden changes in the dam surface gradient (Powledge et al., 1989). This leads to varying levels of erosion along the dam surface that may result in the non-uniform breach morphology, that is, scour holes, reported by (G. G. D. Zhou et al., 2019) (Table 1). The emergence of similar erosional features has also been

21699011, 2022, 10, Downloaded from https://agupubs.onlinelibrary.wiley.com/doi/10.1029/2022JF006664 by Helmholtz-Zentrum Potsdam GFZ, Wiley Online Library on [21/11/2022]. See the Terms and Conditions (https://onlinelibrary.wiley.com/terms-and-conditions) on Wiley Online Library for rules of use; OA articles are governed by the applicable Creative Commons License

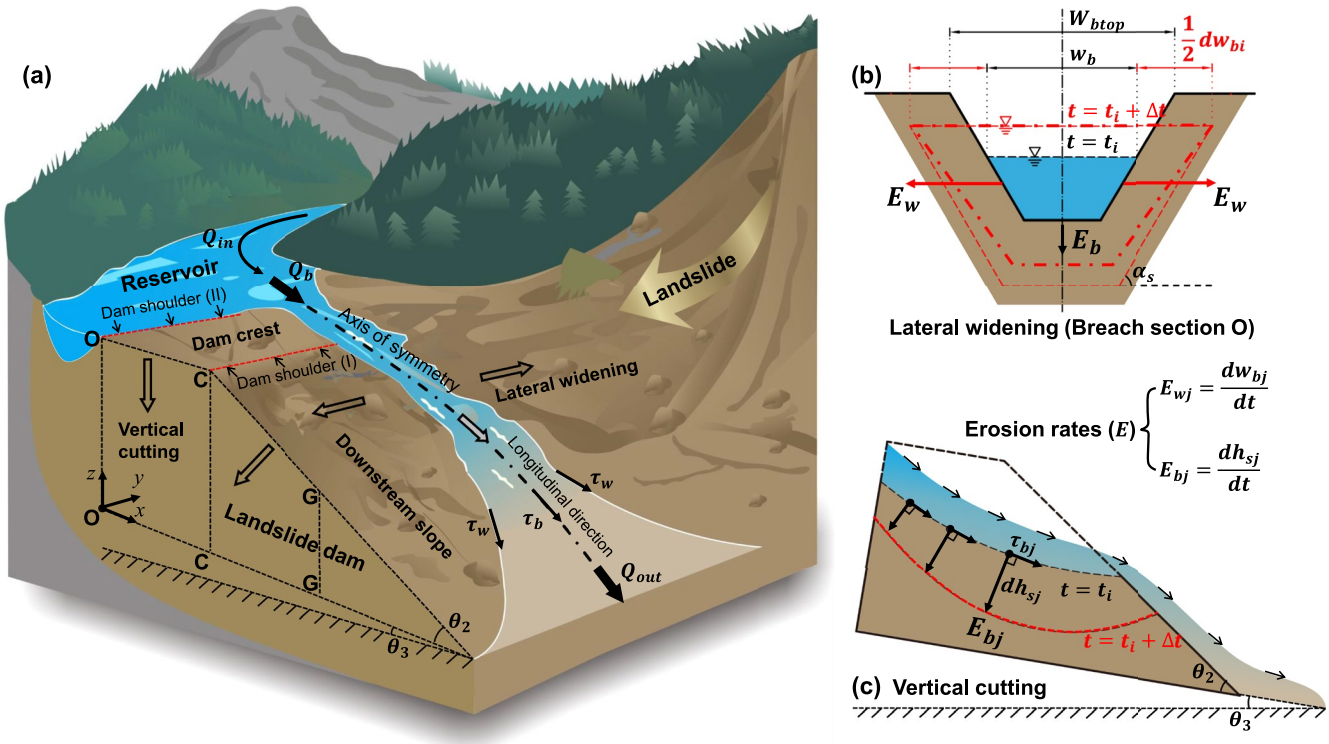

Figure 1. (a) The schematic diagram of the landslide dam failure process adopted in recent literature (Argentin et al., 2021; Korup, 2005; X. Fan et al., 2021). Diagrams of the erosion along (b) the breach width (lateral widening) and (c) the dam height (vertical cutting) from which the sidewall erosion rate E_w and bed erosion rate E_b are calculated, respectively. The trapezoidal shape in panel (b) illustrates the effects of flow velocity gradients along the height wherein the greater velocities at the free-surface result in greater E_w at the top than at the bottom. The dot-dashed line represents varying lateral erosion with time, the dashed line represents slope parallel lateral erosion. W_{btop} is the width of breach channel measured from the top, while w_b is the width of breach channel measured at the water surface. t_i is the time at step i, τ_{bj} is the channel bed shear stress at a certain section j, w_{bj}, and h_{sj} are the erosion width and height, respectively within a certain period Δt. θ_2 is the angle between the dam toe downstream and the river bed, a_s is the side slope angle, and θ_3 is the ambient slope of the river bed. Sections labeled I and II are the downstream and upstream dam shoulders, respectively.

reported in a large-scale landslide dam experiment (with a dam and reservoir volume six orders of magnitude greater than in G. G. D. Zhou et al. (2019)) conducted by the Nanjing Hydraulic Research Institute in China (Figure 2), wherein detailed measurements of the surface evolution were obtained (Zhong et al., 2019). The surface profiles presented in Figure 2c are noticeably similar to the conceptual model proposed by G. G. D. Zhou et al. (2019). Non-uniform surface profiles have also been reported for small-scale flume tests using different dam materials (e.g., Do et al., 2016; Niu et al., 2012) which suggests that this erosional feature is not sensitive to the soil type. Although scour hole formation may also be a common feature in real landslide dams during breaching, no proof of its existence has been reported. This is probably because most dam materials are often washed away after breaching. The lack of evidence from field cases is also due to the turbidity of flows caused by erosion during breaching, which makes the measurement of underwater topography infeasible. Relying on recent experimental evidence, the non-uniform evolution of the breach morphology appears to be a common feature during landslide dam breaches, however, its influence on the discharge and the mechanisms that lead to its formation remain unclear.

In this study, we investigate the mechanisms that lead to the development of non-uniform breach morphologies during landslide dam breaching. To clarify some terminology, the term "dam surface" refers to the portion of the dam over which the overtopping flood flows and is often represented by profiles (drawn in the x–z plane) obtained from the axis of symmetry (details are provided in the Methodology section). "Breach morphology evolution" refers to the change of the shapes of the dam surface profiles with time. Here, we conduct breaching experiments using dams composed of unconsolidated sediments for different inflow discharges. Results are presented on the evolution of the flow discharges and erosion rates. Measurements are compared with numerical simulations that model the different processes that control dam breaching. The numerical model captures the role of the apparent

21699011, 2022, 10, Downloaded from https://agupubs.onlinelibrary.wiley.com/doi/10.1029/2022JF006664 by Helmholtz-Zentrum Potsdam GFZ, Wiley Online Library on [21/11/2022]. See the Terms and Conditions (https://onlinelibrary.wiley.com/terms-and-conditions) on Wiley Online Library for rules of use; OA articles are governed by the applicable Creative Commons License

Table 1
Conceptual Models for Breach Morphology Evolution

Source	Longitudinal profile evolution	Comments
Fread (1988)	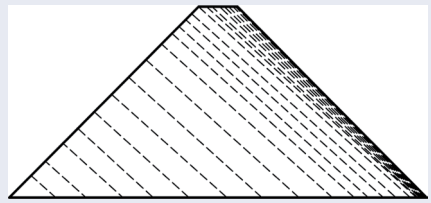	A model for the surface erosion of man-made earthen dams or natural landslide dams made up of cohesive material. Bed erosion is assumed to be uniform along the flow direction. Uniform sidewall erosion is only considered in the breach section
Visser (1999)	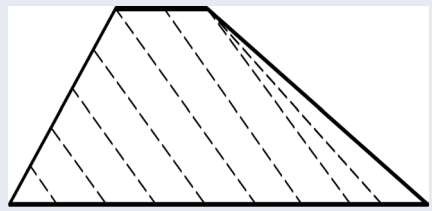	A model for sand dikes made up of non-cohesive sands. Bed erosion is assumed to be uniform but with two linear modes along the flow direction. Uniform sidewall erosion is only considered at the dam crest
Chang and Zhang (2010)	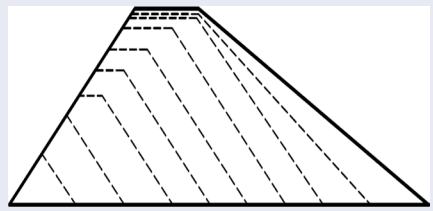	A model for landslide dam failure, wherein the bed erosion is assumed to be uniform but occur step-wise along the flow direction. Uniform sidewall erosion is only considered at a certain cross-section
Yang et al. (2011)	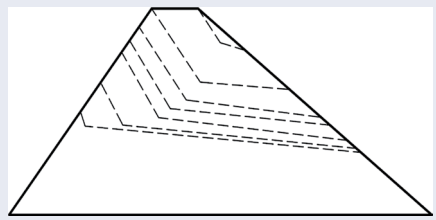	A model for dams made up of natural non-cohesive sands with d_{50} ~1.5 mm, wherein bed erosion is assumed to be uniform but step-wise along the flow direction. Sidewall erosion is ignored
Zhong et al. (2018)	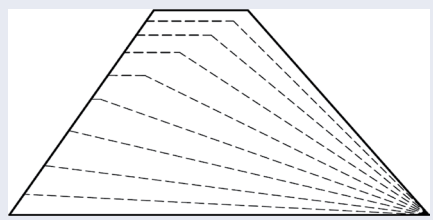	A model for the landslide dam failure wherein the bed erosion is assumed to be uniform but step-wise along the flow direction. Two uniform sidewall erosion modes are assumed at the dam crest and the slope surface, respectively
G. G. D. Zhou et al. (2019)	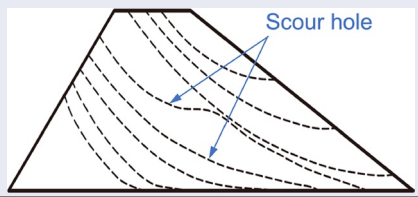	A model for landslide dams composed of non-cohesive soils with d_{50} ~0.85 mm wherein the bed erosion is non-uniform and is characterized by the formation of erosional features (scour holes) along the flow direction. Sidewall erosion is ignored

Note. (i) The shapes of the modeled dams above are drawn based on their original geometry in the literature. (ii) The first three models are proposed or verified according to real dam breach cases while the last three are derived from experiments. (iii) Based on the American Society for Testing and Materials standard, soils are classified as cohesive if the amount of fines, that is, silt and clay-sized materials (Figure S5 in Supporting Information S1) exceed 50% by weight (Mitchell & Soga, 2005). (iv) The dashed lines represent the dam surfaces at different time steps during breaching.

erosion resistance and flood sediment concentration on the evolution of non-uniform surface profiles. We then discuss the mechanisms that control the breach morphology evolution and how the enhanced understanding of the erosion process can improve the modeling of landslide dam failures. This work is an extension of the research presented in G. G. D. Zhou et al. (2019) which recognized the non-uniform dam surface evolution during breaching. It should be mentioned that different from this previous work, which focused mainly on the influence of the

21699011, 2022, 10, Downloaded from https://agupubs.onlinelibrary.wiley.com/doi/10.1029/2022JF006664 by Helmholtz-Zentrum Potsdam GFZ, Wiley Online Library on [21/11/2022]. See the Terms and Conditions (https://onlinelibrary.wiley.com/terms-and-conditions) on Wiley Online Library for rules of use; OA articles are governed by the applicable Creative Commons License

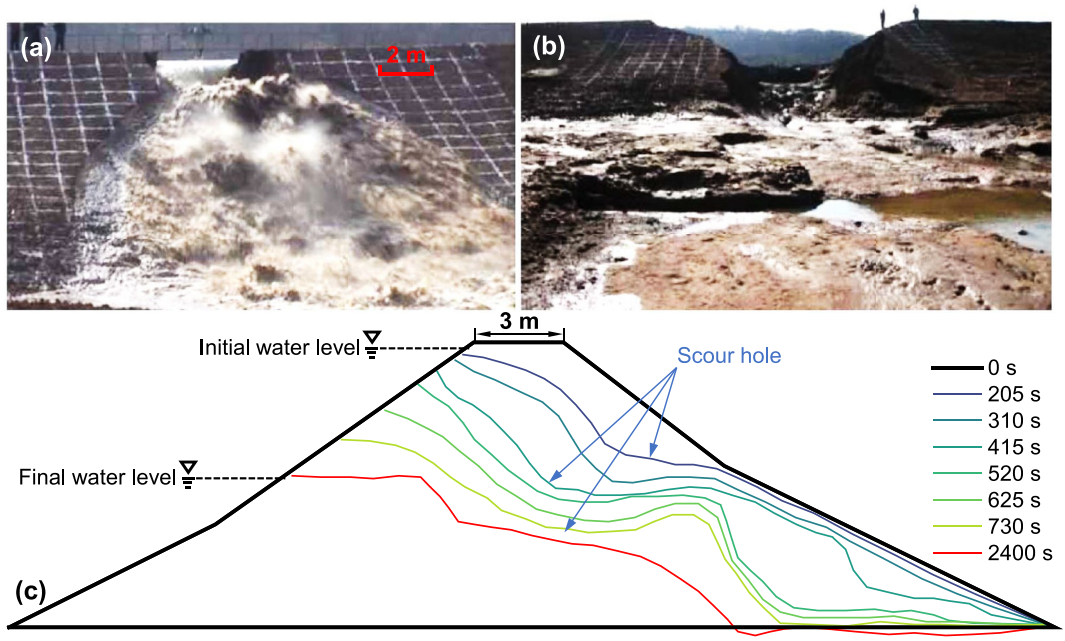

Figure 2. Large-scale overtopping failure experiments of landslide dams composed of cohesive material carried out by the Nanjing Hydraulic Research Institute, China (a) during and (b) after breaching (Zhong et al., 2019). (c) Erosion profiles during dam breach recorded at different time steps (in s). Arrows are pointing at locations where scour holes are evident. (Images are used by permission of the Journal of Geotechnical and Geoenvironmental Engineering, American Society of Civil Engineers).

inflow discharge on the outburst discharge, the work here elucidates the mechanisms that lead to the non-uniform breach morphology.

2. Methodology

2.1. Characterization of the Experimental Set-Up

Hughes (1993) and Iverson (2015) proposed that physical mechanisms derived from model experiments remain valid for their natural counterparts if their geometries scale similarly. The geometry of the model dams here is chosen considering the geometric ratios proposed by Peng and Zhang (2012)—H_d/L_d, $\sqrt[3]{V_d}/H_d$, $\sqrt[3]{V_l}/H_d$—where H_d is the dam height, L_d is the toe to toe dam length of the dam, V_d is the dam volume, and V_l is the lake volume, that express the combined effects of relevant geometric parameters for landslide dams. These geometric ratios have lately been used as construction criteria in modeling landslide dams to ensure that the dams' geometric, kinematic, and dynamic failure processes are similar to real landslide dams (G. G. D. Zhou et al., 2019; J. Y. Zhang et al., 2021; X. G. Jiang et al., 2020). The geometric ratios of the experimental dams fall within the range of values that characterize hundreds of reported landslide dams worldwide (Figure S7 in Supporting Information S1).

The materials used to build the dams control the permeability, stability, compaction, and overall strength of the landslide dam (Casagli et al., 2003). We obtained granular materials with a wide grain size distribution (GSD) from the alluvial fan of the Jiangjia Ravine (103°8′4″ E and 26°14′47″ N) near the Dongchuan Debris Flow Observation and Research Station, Yunnan Province, China. The accumulated GSD is shown in Figure S5 in Supporting Information S1. To simulate the natural accumulation process of uniform and unconsolidated blockages, materials are mixed well prior to being poured into the flume from the same height, thereby forming dams that are graded to the natural repose angle of soils. Manual layer-by-layer compaction is adopted to ensure that the void ratio (0.78–0.80) is consistent with field conditions that are mostly in the range of 0.59–1.11 (Chang & Zhang, 2010). The dams are then molded into the desired geometry. Moreover, the use of in-situ materials ensures that the initial (gravimetric) moisture contents (6% ± 0.5%) of the model dams are comparable to those of natural landslide dams. Despite the measures taken to ensure the model dams' consistency with their natural counterparts,

21699011, 2022, 10, Downloaded from https://agupubs.onlinelibrary.wiley.com/doi/10.1029/2022JF006664 by Helmholtz-Zentrum Potsdam GFZ, Wiley Online Library on [21/11/2022]. See the Terms and Conditions (https://onlinelibrary.wiley.com/terms-and-conditions) on Wiley Online Library for rules of use; OA articles are governed by the applicable Creative Commons License

Fan et al. (2020) pointed out that laboratory-scale set-ups only represent dams that form through slides or flows of unconsolidated sediments. Such dams make up only a small subset of those that form in nature. Nevertheless, the mechanisms of surface erosion that we determine here are also manifested in other natural slopes other than landslide dam surfaces and may hence be applicable to dams that form through different depositional processes.

2.2. Experimental Set-Up

Experiments are conducted in a large experimental flume that is 45 m long, 0.7 m wide, 1.4 m deep, and is inclined at 12° from the horizontal (Figure 3a). The flume is connected to a water container, with a maximum capacity of 12 m^3, through a steel tube with a manual hydro valve. The inflow discharge (Q_{in}) can be accurately estimated by the water level gauge positioned behind two sharp-crested weirs (G. G. D. Zhou et al., 2015), located at the head of the flume ~20 m away from the upstream dam toe. The turbulent inflow subsides after passing through two rows of saw-teeth which effectively improves the estimation accuracy of the inflow discharge based on the widely accepted sharp-crested weir model (G. G. D. Zhou et al., 2015). An energy dissipation pool at the bottom of the test flume (near the second sharp-crested weir) further minimizes the flow turbulence. Reinforced glass windows (1.5 m in width) with reference grids (0.1 × 0.1 m) are installed along the right side of the flume allowing for the observation of the longitudinal dam profiles (Figure 3c). The glass window serves as the dam's axis of symmetry. Although border effects are unavoidable in semi-symmetric set-ups, we minimize their influence by using large inflow discharges and a large ambient inclination (12°). After constructing the dam according to the desired geometry, a rectangular notch (0.05 × 0.1 m), adjacent to the glass sidewall, is excavated on the dam crest (Figure 3b) to ensure that overtopping is initiated at the same location and encourages the repeatability of the test cases. The location of the notch here is consistent with the literature involving semi-symmetric dams (Balmforth et al., 2008; Coleman et al., 2002) but it should be mentioned that other works position the notch at the center axis of the modeled dam (e.g., Hanson et al., 2005; Walder et al., 2015; Walsh et al., 2021).

Four test cases corresponding to different inflow discharges $Q_{in} = 2.0, 3.0, 5.3, 6.9 \times 10^{-3}$ m^3/s labeled with Test IDs C-Q 2.0, C-Q 3.0, C-Q 5.3, and C-Q 6.9, respectively, are conducted to study the influence of the inflow

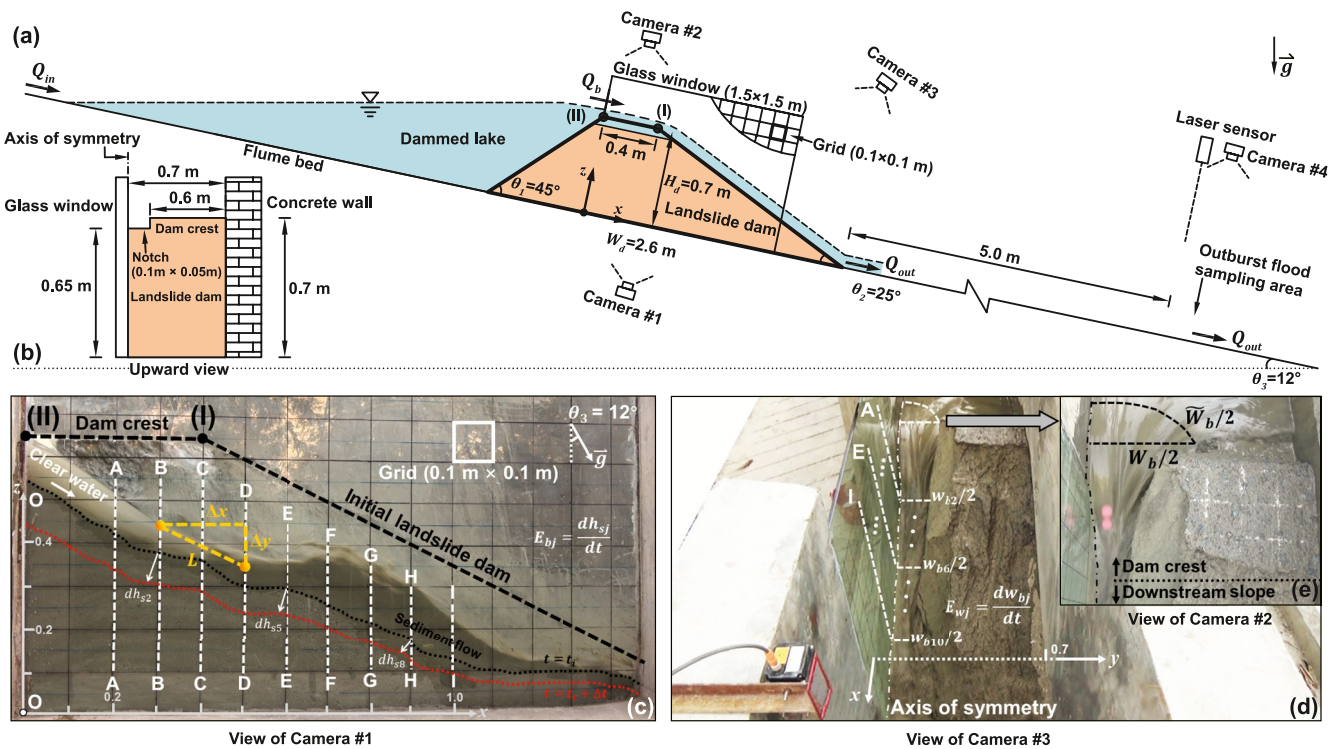

Figure 3. Schematic diagram of the experimental set-up with the exact dimensions as viewed from the (a) side and from the (b) front. (c) The side view of the dam (from Camera #1) is divided into sections. (d) Top view of the dam (from Camera #3) and a (e) zoomed-in image of the dam crest during breaching. W_b is the width of the breach channel and $\tilde{W}_b$ is the arch length of the breach. Sections I and II are the downstream and upstream dam shoulders, respectively.

21699011, 2022, 10, Downloaded from https://agupubs.onlinelibrary.wiley.com/doi/10.1029/2022JF006664 by Helmholtz-Zentrum Potsdam GFZ, Wiley Online Library on [21/11/2022]. See the Terms and Conditions (https://onlinelibrary.wiley.com/terms-and-conditions) on Wiley Online Library for rules of use; OA articles are governed by the applicable Creative Commons License

on the landslide dam breaching process. Each test is performed at least twice. Three video cameras (SONY FDR-AX40, 1,440 × 1,080 pixels, 25 fps) monitor the dam breaching process from different vantage points (Figure 3). Camera #1 monitors the change of the flow depths based on the reference grids imprinted on the glass window (Figure 3c). The grids divide the window into nine sections labeled A–I which serve as reference points wherein E_b, E_w, and the shear stress (τ) are evaluated. The interface between the breach flow and the dam body is defined as a boundary between a moving flow and a static layer defining the motionless dam. This interface is determined manually from image sequences representing certain periods of interest. Thus, camera #1 can also capture the erosion depth change (h_{sj}) with time, and the bed erosion rate (E_b). The flow velocity (u_f) is determined from the trajectory of tracer particles dropped onto the surface of the breaching flow. The distance $L = \sqrt{\Delta x^2 + \Delta y^2}$, where Δx and Δy are changes in the particles' x and y positions, traveled by the particles within a specific timeframe is measured using an open-source image processing software, ImageJ (Schneider et al., 2012) (Figure 3c). We also evaluate the flow velocity at different length scales ($\Delta x = 0.1$, 0.2, 0.4 m). A small $\Delta x = 0.1$ m results in significant fluctuations in the estimation of u_f, whereas a large $\Delta x = 0.4$ m results in diminished estimation resolution. A moderate $\Delta x = 0.2$ m is therefore used to measure u_f along the longitudinal dam profile. Camera #2 monitors the channel width change (w_{bj}), whose measurement is calibrated against the flume width (0.7 m) (Figure 3e). The breach discharge (Q_b) is defined as the volume of water flowing through a given section per unit time (Szymkiewicz, 2010). Q_b is calculated at the breach cross section O using the Open Channel Flow Assumption (Chanson, 2004):

$$Q_b = \overline{\alpha} \times \gamma \times u_f \times h_f \times W_b \tag{1}$$

where W_b is the channel width, u_f is the flow velocity, and h_f is the flow depth. Note that, different from the illustration in Figure 1a, Q_b is measured at a fixed point since the concrete wall prevents us from determining the upstream dam shoulder (section II) that has migrated upwards due to erosion. Nevertheless, this hidden portion makes up only a small fraction of the dam body and has little effect on the measurement of Q_b. The constant $\overline{\alpha} = 0.71$ is the mean parabolic coefficient, and $\gamma = 2/3$ is the ratio between the surface velocity and mean velocity. The value of $\overline{\alpha}$ is obtained from the mean of values previously calculated for 37 dams having different geometries and soil properties. Since this value is relevant only to the breach discharge, its accurate determination does not change the conclusions drawn from this work. Details on the estimation of $\overline{\alpha}$ and γ are provided in Text S1 in Supporting Information S1. The w_{bj} is measured along the sloping surface from the footage of Camera #3 (Figure 3d), from which the lateral widening rate (E_w) can be obtained. Downstream, ~5 m from the foot of the dam, the outburst flow velocity and height, from which Q_{out} is calculated (same with Q_b), are measured from images obtained by Camera #4 and a laser sensor (Leuze, ODSL 30/V-30MS12) with a resolution of ±1 mm, respectively. We mention that the same experimental setup and procedures have been adopted in our previous work (G. G. D. Zhou et al., 2019; M. J. Zhou et al., 2019). However, in this work, the results obtained from the experiments are reanalyzed to provide a deeper understanding of the processes that control the surface evolution of landslide dam failure that has been largely ignored in the previous research.

2.3. Theoretical Background of the Numerical Model

An overtopping flood can be simplified into a homogenous incompressible fluid flowing down an inclined erodible surface. The flow can be defined by the following mass and momentum equations:

$$\frac{\partial \rho_f}{\partial t} + \nabla \cdot (\rho_f \boldsymbol{u}) = \Delta m, \tag{2}$$

$$\frac{\partial \rho_f \boldsymbol{u}}{\partial t} + \nabla \cdot (\rho_f \boldsymbol{u} \otimes \boldsymbol{u}) = \rho_f \boldsymbol{g} + \nabla \cdot \boldsymbol{T} + \Delta \boldsymbol{M},$$

where ρ_f is the flow density, $\boldsymbol{u}$ is the flow velocity vector, and $\boldsymbol{g}$ is the gravitational acceleration. $\boldsymbol{T}$ is the stress tensor ($\boldsymbol{T} = -P\boldsymbol{I} + \boldsymbol{\tau}$) where $\boldsymbol{I}$ is the unit tensor, P is the normal component, and $\boldsymbol{\tau}$ is the deviatoric component. For simplicity, these stress components are referred to as the pressure and the shear stress respectively. Δm is the rate of mass change of the overtopping flow that results from entrained sediment materials and $\Delta \boldsymbol{M}$ is the corresponding change of flow momentum. Since the flow is incompressible, $\partial \rho_f / \partial t$ can be set to zero. The mixture flow is assumed to be a shallow water flow because its characteristic length greatly exceeds the flow depth (Savage & Hutter, 1989). A depth-averaged form of Equation 2 can be written as:

21699011, 2022, 10, Downloaded from https://agupubs.onlinelibrary.wiley.com/doi/10.1029/2022JF006664 by Helmholtz-Zentrum Potsdam GFZ, Wiley Online Library on [21/11/2022]. See the Terms and Conditions (https://onlinelibrary.wiley.com/terms-and-conditions) on Wiley Online Library for rules of use; OA articles are governed by the applicable Creative Commons License

$$\frac{\partial h_f}{\partial t} + \frac{\partial (h_f u_f)}{\partial x} = \frac{\rho_s}{\rho_f}\frac{\partial h_s}{\partial t}(1-p), \tag{3a}$$

$$\frac{\partial h_f C_s}{\partial t} + \frac{\partial (h_f u_f C_s)}{\partial x} = \frac{\rho_s}{\rho_f}\frac{\partial h_s}{\partial t}(1-p), \tag{3b}$$

$$\frac{\partial (h_f u_f)}{\partial t} + \frac{\partial}{\partial x}\left(h_f u_f^2 + \frac{1}{2}k_{ap} g \sin\theta_b h_f^2\right) = g\sin\theta_b h_f - f_{bs} + u_f \frac{\rho_s}{\rho_f}\frac{\partial h_s}{\partial t}(1-p), \tag{3c}$$

where h_f, u_f, and $h_f u_f$ represent the flow depth, the depth-averaged flow velocity, and the flow discharge in the x direction, respectively. g is the gravitational acceleration. The flow density is calculated as $\rho_f = C_s\rho_s + (1 - C_s)\rho_w$ where $C_s = h_s/h_f$ is the volumetric sediment concentration, ρ_s and ρ_w are the density of the sediment and water having fixed values of 2,650 and 1,000 kg/m^3 respectively. The source terms on the right-hand side of the mass balance Equations 3a and 3b denote the mass change rate due to bed erosion. In Equation 3c, f_{bs} represents the basal frictional resistance calculated from Manning's formula, p is the bed porosity, and k_{ap} is the lateral earth pressure coefficient which is equal to one in this study. Further details on the model setting parameters are listed in Table S2 in Supporting Information S1.

A natural extension of the Lax-Friedrich first-order central differencing scheme is used to solve the hyperbolic equation system above. This scheme avoids characteristic decomposition since we do not need to solve Riemann problems (Nessyahu & Tadmor, 1990). The excessive Lax-Friedrich scheme is a second or higher-order resolution Riemann-solver-free family of central differencing schemes (G.-S. Jiang et al., 1998; Kurganov & Tadmor, 2000; Sweby, 1984). The resolution of the simulation domain is 0.01 m. Our numerical model setup satisfies the Courant-Friedrichs-Lewy condition, thus ensuring numerical stability in each time step.

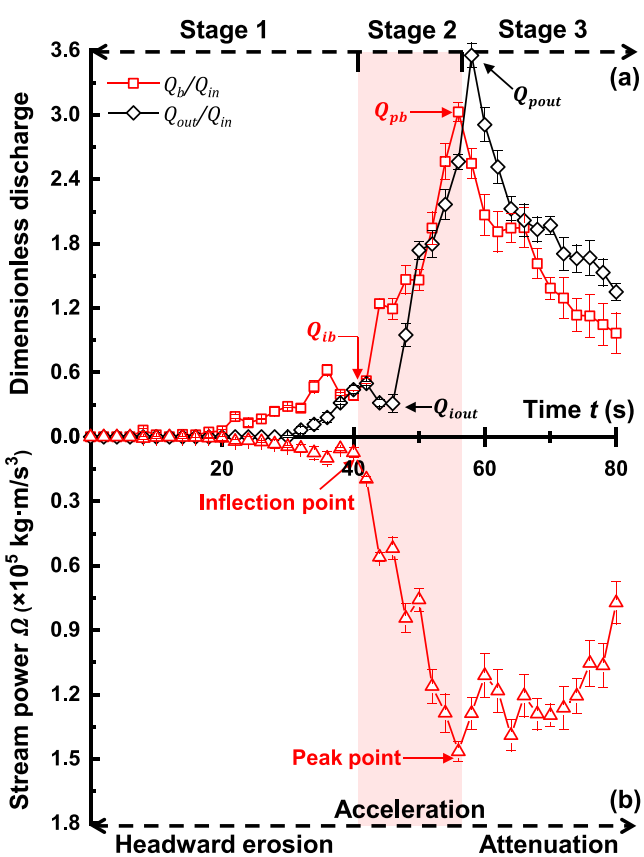

Figure 4. Hydrograph of a sample case C-Q 5.3 showing the change of the (top) dimensionless breach Q_b/Q_{in} and outburst Q_{out}/Q_{in} discharges, and (bottom) stream power Ω with time at x =0 m. Q_{in} is the inflow discharge. Stages of the hydrograph are characterized by the inflection (Q_{ib} and Q_{iout}) and peak points (Q_{pb} and Q_{pout}) of the breach discharge, outburst discharge, and stream power. Error bars are measurement standard deviations.

3. Results

3.1. Dam Breach Hydrographs

The hydrographs of the dimensionless breach discharge Q_b/Q_{in} and outburst discharge Q_{out}/Q_{in} are presented in Figure 4a. The $t = 0$ s is the time when the flow starts to travel along the notch and reaches the dam shoulder (Figure 3a). After a certain period of time, both dimensionless discharges abruptly increase and reach peak values. The time at which this increase is observed is called the inflection point and is determined for both the breach Q_{ib} and outburst Q_{iout} discharges. Peak breach and outburst discharge points are labeled Q_{pb} and Q_{pout} respectively. Q_b starts to increase at $t = 20$ s, while Q_{out} increases at $t = 30$ s. The time lag between the two hydrographs can be attributed to the infiltration within the loose and unconsolidated dam. Q_{out} is minimal when Q_b has just begun to increase since a large portion of the water infiltrates into the landslide dam. This time lag becomes smaller as Q_b increases. There is a 6-s time difference observed between inflection points, while there is only a 2-s time lag between peak points (Figure 4a). A larger Q_b usually implies greater flow velocities since there is little change in flow height during this stage (G. G. D. Zhou et al., 2019). More sediment is transported at a higher rate thus resulting in shorter lag times. Q_{pout} is greater than Q_{pb} since outburst floods include more entrained sediments. Indeed, it can be observed in Figure 3c that the breaching flood starts off as a clear water flow at the dam shoulder (II) and becomes increasingly turbid further downstream indicating a gradual increase in the sediment concentration C_s. The role of C_s in the erosion process will be made clear in the successive sections.

The breach discharge Q_b can be representative of the dam breaching hydrodynamics as well as the erosive capacity of the water flow. The stream power,

21699011, 2022, 10, Downloaded from https://agupubs.onlinelibrary.wiley.com/doi/10.1029/2022JF006664 by Helmholtz-Zentrum Potsdam GFZ, Wiley Online Library on [21/11/2022]. See the Terms and Conditions (https://onlinelibrary.wiley.com/terms-and-conditions) on Wiley Online Library for rules of use; OA articles are governed by the applicable Creative Commons License

given by Bagnold (1966), (i.e., $\Omega = \rho_w g Q_b \theta_b$, where ρ_w is the clear water density, 1,000 kg/m^3, g is the gravitational acceleration, and θ_b is the slope of the channel bed) expresses the dissipation rate of the potential energy against the bed and sidewalls per unit length and quantifies the work needed to erode and transport sediment downstream (Haschenburger & Church, 1998). The stream power is widely used to describe the flood erosive capacity over the dam surface (Annandale, 2006). The dam failure process is designated into three stages according to the evolution of Q_b and Ω (Figure 4). Stage 1 spans from the initiation time to the inflection point of Q_b and Ω (t =0–40 s). At this stage, erosion is weak, and the erosion point slowly migrates back upstream from the dam shoulder (from Points I to II in Figure 3c). Stage 2 spans the inflection point to the peak point of Q_b and Ω (t =40–56 s). During this stage, the erosive capacity increases rapidly due to the sudden increase in Q_b caused by the sudden release of dammed water (G. G. D. Zhou et al., 2019). The increased discharge erodes and entrains larger volumes of sediment. The enhanced erosion induces steep channel inclinations along the dam surface which randomly collapse under the continuous shear of the incoming flood above. At Stage 3, the dammed water runs out and the erosive capacities start to decay up until the end of the dam breaching (t = 56–80 s). In the literature, these stages are also referred to as the headward, accelerated, and attenuated erosion stages (G. G. D. Zhou et al., 2019). Note that other works have also designated the dam breach hydrograph into stages using different criteria (i.e., outburst discharge or erosion morphology) other than the breach discharge and stream power (Peng et al., 2021; Ruan et al., 2021). Movies showing the erosion process are provided in References in Supporting Information S1.

3.2. Erosion Mechanisms

As the flood travels from the breach crest to the dam toe, it displaces and carries the sediments from the dam surface. The dam crest is a hydraulic control structure that acts as a natural weir. In other words, it controls the breach flow discharge and the erosion dynamics during dam breaching and thus the outflow discharge (Walder et al., 2015; Walsh et al., 2021). Here, we measure the erosion at the discrete cross-sections along the sloping surface to gain insight into the mechanisms that influence the evolution of the dam morphology.

3.2.1. Effects of Flow Discharge on Erosion Rates

The dam crest acts as a broad-crested weir that controls the flow discharge during breaching. However, different from the non-erodible weirs that are typically used to control the discharge of incoming flows (Castro-Orgaz et al., 2022; Hager & Schwalt, 1994; Haun et al., 2011), the dam crests of landslide dams are erodible and their evolution affects the flow conditions downstream. As shown in Figure 4, the changes in the dam crest are reflected in the evolution of Q_b, that is, the wider and deeper the dam crest becomes due to the erosion of breach flow, the greater the amount of dammed water is released until the water supply is depleted (Singh & Scarlatos, 1988; Walder et al., 2015). In this work, we are more interested in the erosion and breach morphology evolution of the sloping surface resulting from the variations in the breach discharge, hence the evolution of the dam crest geometry itself will no longer be discussed in detail.

Figure 5a shows the temporal profiles of the bed E_b and sidewall E_w erosion rates respectively, calculated in the breach section. The erosion rates are plotted alongside the breach (red) and outburst (blue) discharges. Both E_b and E_w are observed to exhibit a similar trend as Q_b, they initially increase prior to decreasing after reaching a peak value, although both reach peak values at different times. Specifically, E_b reaches a peak value at 62 s, while E_w is almost synchronized with Q_b having peak values at 54 and 56 s, respectively. This coincidence indicates that the breach discharge is better correlated with lateral widening than it is with vertical cutting. In addition, we also observe that the erosion rates at Stage 2 almost remain constant with time while the flow discharges increase rapidly. Similar results can also be found in Walsh et al. (2021) which involved dams composed of uniformly sized sand. We further plot the temporal evolution of erosion rates in sections C (Figure 4b) and G (Figure 4c) along the flow direction in which different results are observed: E_b is up to two or three times greater than E_w at both sections. The higher erosion rates along the bed, relative to the lateral directions, are likewise observed in the experiments of Turowski et al. (2006) and Yang et al. (2011). We also find that the changes in the erosion rates with time are non-uniform in the different sections considered (sections O, C, and G), which may be caused by the non-uniform erosion of the flow, the varying resistance of the channel bed, or both (G. G. D. Zhou et al., 2019). Details of the evolution of erosion rates and mechanisms are further studied in the successive sections.

21699011, 2022, 10, Downloaded from https://agupubs.onlinelibrary.wiley.com/doi/10.1029/2022JF006664 by Helmholtz-Zentrum Potsdam GFZ, Wiley Online Library on [21/11/2022]. See the Terms and Conditions (https://onlinelibrary.wiley.com/terms-and-conditions) on Wiley Online Library for rules of use; OA articles are governed by the applicable Creative Commons License

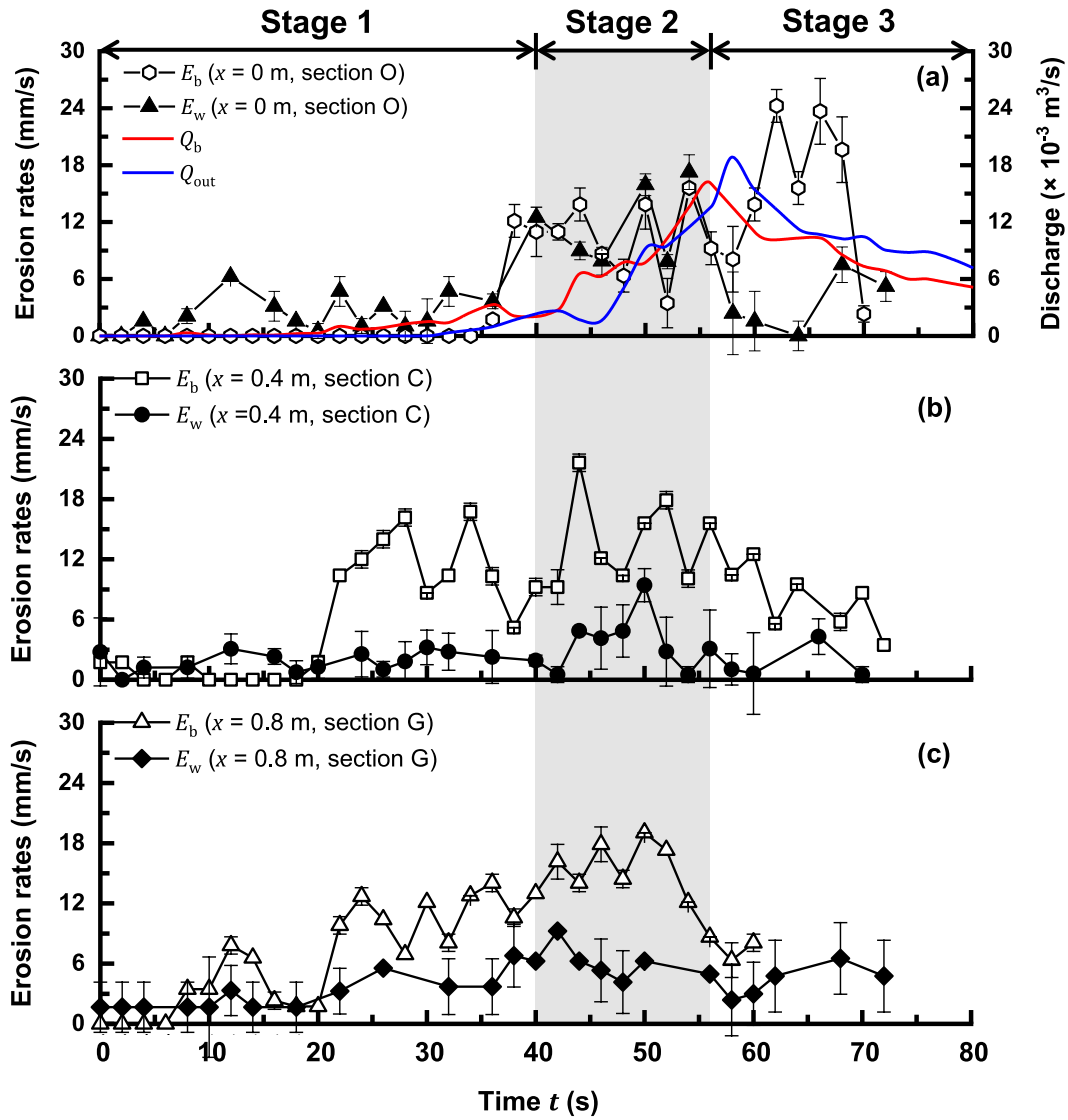

Figure 5. Erosion rates as functions of time during dam breaching of representative test case C-Q 5.3. (a) The sidewall erosion (lateral widening) at the breach better coincides with the flow discharges. Temporal variation of the (b) bed and (c) sidewall erosion rate at Sections C and G, respectively.

3.2.2. Longitudinal Distribution of Erosion Rates

Here, we study the relationship between erosion rates and the shear stresses along the flow direction. Dam surface erosion can be directly quantified using the linear erosion equation proposed by Partheniades (1965), which has been widely applied for sediment erosion (Fraccarollo & Capart, 2002; Graf, 1984; Howard, 1994; Iverson, 2012; Sheng & Lick, 1979). These equations are written as:

$$E_b = K_{db}\left(\tau_b - \tau_{cb}\right),$$

$$E_w = K_{dw}\left(\tau_w - \tau_{cw}\right), \tag{4}$$

for erosion along the vertical and lateral directions, respectively. K_{db} and K_{dw} are dimensional constants of erodibility; τ_b and τ_w are the shear stresses exerted by the fluid on the channel bed and sidewall. τ_{cb} and τ_{cw} are the apparent erosion resistances, also known in the literature as critical shear stress (Cheng, 2004; Chepil, 1959;

21699011, 2022, 10, Downloaded from https://agupubs.onlinelibrary.wiley.com/doi/10.1029/2022JF006664 by Helmholtz-Zentrum Potsdam GFZ, Wiley Online Library on [21/11/2022]. See the Terms and Conditions (https://onlinelibrary.wiley.com/terms-and-conditions) on Wiley Online Library for rules of use; OA articles are governed by the applicable Creative Commons License

Paphitis, 2001). The vertical flow shear stress τ_b can be determined using Manning's equation (Cantero-Chinchilla et al., 2016; Wu, 2013; Z. Y. Chen et al., 2015):

$$\tau_b = \frac{\rho_f g n^2 u_f^2}{h_f^{1/3}}, \tag{5}$$

where ρ_f is the flow density, g is the acceleration due to gravity, n is the Manning coefficient, and u_f is the flow velocity. The flow depth h_f is also known as the hydraulic radius in the literature, especially when flow depth is much smaller than breach width (Dazzi et al., 2019; Guo & Jin, 1999). The lateral shear stress τ_w is calculated as:

$$\tau_w = \varepsilon \tau_b, \tag{6}$$

where ε is a function of the flow width-depth ratio w_b/h_f which ranges between 0.537 and 1.479 in this study (Figure S4 in Supporting Information S1). A detailed definition of ε can be found in Text S2 in Supporting Information S1. Note that although alternative expressions for the erosion rate have also been presented in the literature, obtained empirically (Takahashi, 1991) or theoretically (Fraccarollo & Capart, 2002), most of them can be generalized into the basic framework presented in Equation 4 (G. G. D. Zhou et al., 2020).

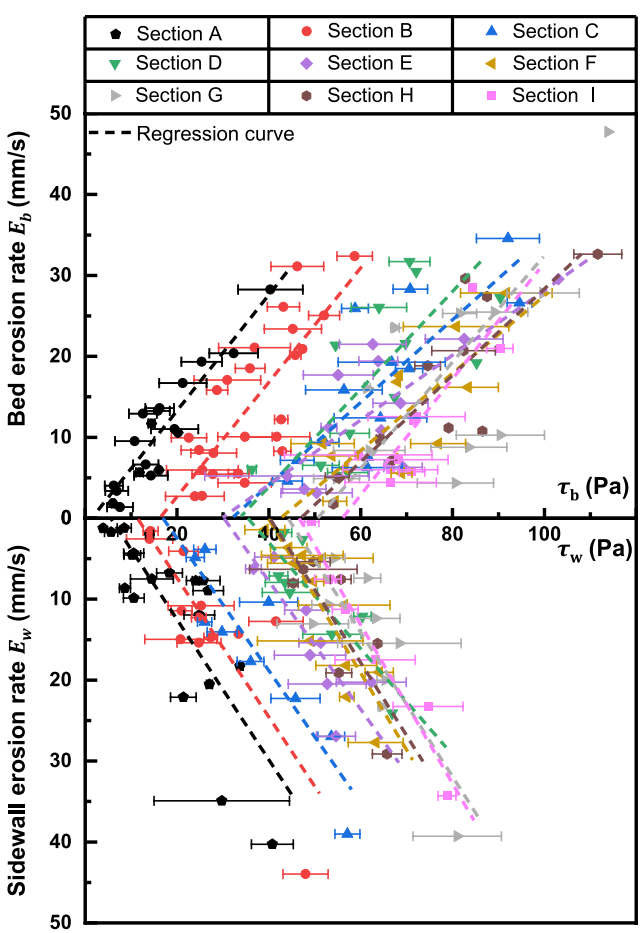

Figure 6. Relationships between erosion rate and shear stress in the (top) vertical and (bottom) lateral directions at the different sections (A–I) during Stages 2 and 3 for all experiments. Dashed lines are best fits provided by Equation 4. Different colors represent different sections. The calculated bed and sidewall shear stresses are obtained based on Equations 5 and 6, respectively. Error bars for shear stress express the measured standard deviations.

Figure 6 shows the erosion rate versus the shear stress along the vertical (E_b, τ_b)and lateral (E_w, τ_w)directions of four different test cases at different sections of the dam. The erosion rates appear to vary linearly with the shear stress although significant scatter is observed. The dashed lines are best fits obtained from Equation 4. Similar linear relationships have also been reported by Fujisawa et al. (2008) and Knapen et al. (2007) from both field observations and experiments. Note that only data points corresponding to Stages 2 and 3 are considered in this analysis since the erosion in Stage 1, as shown in Figures 4 and 5, is much weaker and depends only on the small variations of the overtopping flow velocities. More details on the fitting can be found in Table S1 in Supporting Information S1.

The slopes of the best fit lines in Figure 6 correspond to K_{db} and K_{dw} for the erosion along the vertical and lateral directions. Figure 7 shows that both erodibilities do not change systematically along the dam surface but instead fluctuate around an average value. For convenience in the subsequent analysis, we take the mean of the fluctuating values (dashed lines) and get two distinct soil erodibilities for the vertical and lateral directions (Figure 7a). Note that the mean K_{dw} is slightly larger than K_{db}, which is apparently inconsistent with the erosion rate data (Figure 5) wherein E_b is greater than E_w both at the dam crest and the downstream surface. E_b is greater than E_w because the measured basal shear stresses are generally larger than those measured at the walls (Figure S4 in Supporting Information S1). This implies that the erosion rate and its evolution along the dam surface are more sensitive to the shear stress than they are to the soil erodibility.

The intercepts of the best fitting lines on the abscissa in Figure 6 are the apparent erosion resistance of sediments (τ_c) (G. G. D. Zhou et al., 2019), defined separately for the channel bed (τ_{cb}) and the sidewalls (τ_{cw}). The apparent erosion resistance may be related to the soil properties (e.g., plasticity index, mean particle size, repose angle, void ratio, etc.), flow properties (e.g., sediment concentration, the kinematic viscosity of flow, etc.), and other hydraulic parameters (e.g., the relative density of particles submerged in the flow, the acceleration of gravity or local channel slope, etc.) (D. Chen et al., 2018; G. G. D. Zhou et al., 2019; H. W. Zhang, 2012; Wainwright et al., 2015; Wu et al., 2018). Figure 7b shows that τ_{cb} and τ_{cw} are almost identical (most data points fall within a 95% confidence interval) and linearly increase with the longitudinal distance.

21699011, 2022, 10, Downloaded from https://agupubs.onlinelibrary.wiley.com/doi/10.1029/2022JF006664 by Helmholtz-Zentrum Potsdam GFZ, Wiley Online Library on [21/11/2022]. See the Terms and Conditions (https://onlinelibrary.wiley.com/terms-and-conditions) on Wiley Online Library for rules of use; OA articles are governed by the applicable Creative Commons License

The deviation of the data points from the best fit lines can be quantified by the ratio of the Root Mean Squared Error ($RMSE$) and the Standard Deviation (SD) (Figure 7c). The $RMSE/SD$ ratio quantifies the deviation of the measured E_b and E_w from the best-fit lines relative to the spread of the erosion rate data around their mean values at different cross-sections. Specifically, $RMSE/SD < 1$ means that the deviation from the best-fit line (dashed lines in Figure 6) is less than the random scatter of the data set, while $RMSE/SD \geq 1$ means that the data is simply randomly distributed around the best fit (Bruce et al., 2016). The latter condition means that the best-fit line does not correctly define the relationship between the shear stress and erosion rate. Figure 7c shows that all $RMSE/SD$ are less than 1. This indicates that despite the scatter observed in Figure 6 for both erosion rates, the deviation of the measured erosion rates from the predictions of Equation 4 are still much less than the random scatter of the data set at each section.

To further explore the correlation between the erosion rate and shear stress, the calculated (Equation 4) and measured basal (Figure 1c) and lateral (Figure 1b) erosion rates are plotted alongside their corresponding shear stresses (Equations 5 and 6) under different inflow discharges in Figure 8. These data points are obtained during Stage 2 of the breaching process. Note that in contrast to Figure 6, here we aim to see the similarity of the longitudinal distributions of the abovementioned quantities. It can be observed that both the calculated and measured erosion rates follow a similar pattern and vary consistently with the shear stress, further indicating a close correlation between the two variables. E_b varies similarly with E_w so their peak values are measured at the same positions along the dam. Similar behavior is observed with the longitudinal evolution of τ_b and τ_w. Since K_d is a constant value for each case along the flow direction (Figure 7a), this implies that the difference between shear stress (τ) and apparent erosion resistance (τ_c) controls the erosion rates and thus the evolution of the dam morphology based on Equation 4 (J. P. Johnson & Whipple, 2010). It is also noted that some slight deviations between the calculated and measured values can be observed, which is visualized in Figure 8e. It can be noticed in Figure 8e that some measured data points can be twice as large as the calculated values in some regions. However, in most cases, the deviation between the two quantities is less than 50%. This deviation may be due to systematic and random errors in the measurement of u_f and h_f, or the estimation of K_d and τ_c. Even then, Figure 8 demonstrates that the erosion mechanisms are consistent both in the vertical and lateral directions across different inflow discharges.

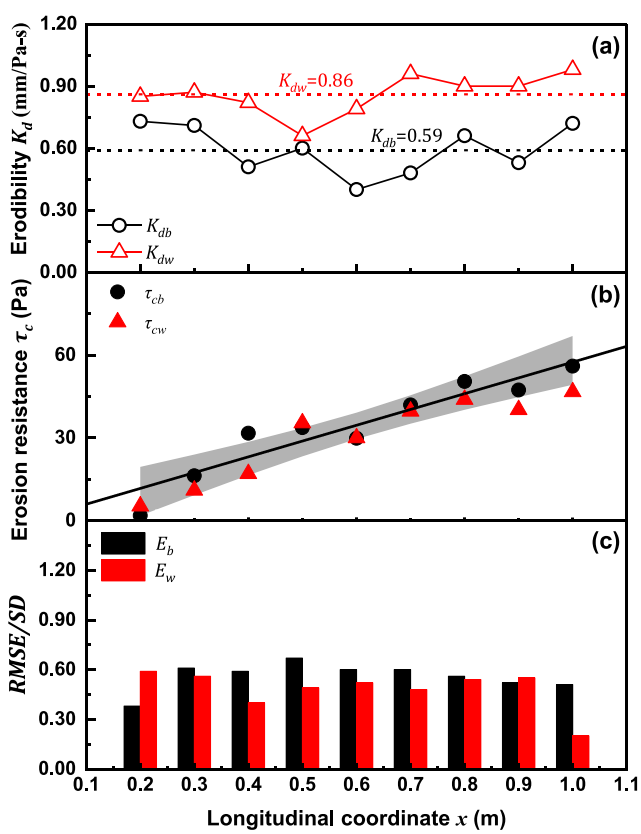

Figure 7. The (a) distribution of the soil erodibility along the vertical (black points) and lateral (red points) directions. The K_{dw} and K_{db} are the mean of the erodibilities along the lateral and vertical directions represented by dashed lines. (b) The apparent erosion resistance τ_c along the bed (black circles) and lateral (red triangles) directions. The black line is a linear regression curve defined by $\tau_c = 57.36x + 0.25$. The gray band represents a 95% confidence interval. (c) The ratio of the Root Mean Squared Error ($RMSE$) and Standard Deviation (SD) quantifying the scatter of the of bed and sidewall erosion rates from the best fit in Figure 6.

3.2.3. Physical Interpretation of the Distribution of Erosion Rates

Most previous studies assume that dam failure occurs uniformly along the dam surface (Table 1). In contrast, results in our study show that dam failure profiles can vary significantly due to the nonlinear change of the shear stresses and the linear increase of the apparent erosion resistance along the flow direction. Since the shear stress is mainly controlled by the flow velocity (Equation 5), we argue that the non-uniform evolution of the erosion profiles is due to local variations in the flow velocity during dam breaching. According to the kinetic energy theorem, the theoretical velocity of a tracer particle moving along the dam surface can be written as:

$$u_{i+\Delta t}^2 - u_i^2 = 2L\,(g \sin\theta_b - \mu_k g \cos\theta_b) = 2x\,(g \tan\theta_b - \mu_k g)\,, \qquad (7)$$

where u_i is the velocity of a tracer particle at any time step i; θ_b is the channel bed inclination angle; μ_k is the dynamic friction factor; x is the travel distance projected onto the horizontal axis; and L is the travel distance. Assuming that $u_i = 0$ m/s at $t = 0$ s, Equation 7 can be simplified as:

$$u_{i+\Delta t}^2 = 2x\,(g \tan\theta_b - \mu_k g) \qquad (8)$$

In pure water, the μ_k between fluid particle and a soil bed is relatively small, varying from 0.01 to 0.02 based on the Moody Diagram (LaViolette, 2017), and can therefore be neglected (mean gradient of local channel bed here is 0.46) reducing Equation 8 into:

21699011, 2022, 10, Downloaded from https://agupubs.onlinelibrary.wiley.com/doi/10.1029/2022JF006664 by Helmholtz-Zentrum Potsdam GFZ, Wiley Online Library on [21/11/2022]. See the Terms and Conditions (https://onlinelibrary.wiley.com/terms-and-conditions) on Wiley Online Library for rules of use; OA articles are governed by the applicable Creative Commons License

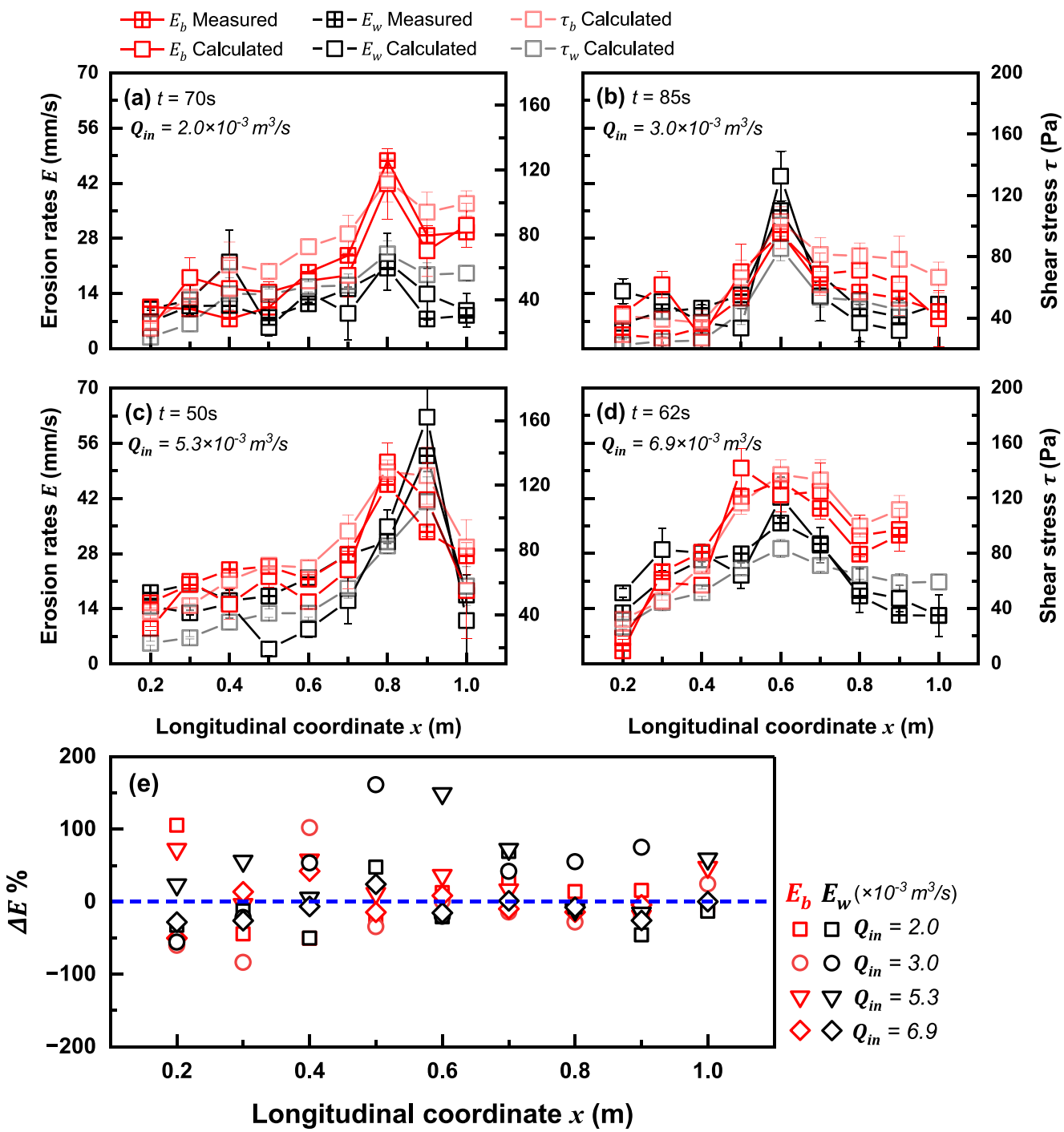

Figure 8. (a–d) The evolution of the bed and sidewall erosion rates along the flow direction in the (red) vertical and (black) lateral directions for different inflow discharges. The measured erosion rates are defined in Figures 1b and 1c, while calculated values are obtained using Equation 4. The calculated shear stress is defined by Manning's Equations 5 and 6 for bed and sidewalls, respectively. (e) The percentage difference between measured and calculated quantities $\Delta E\% = (\text{Measured} - \text{Calculated})/\text{Calculated} \times 100$ for different inflow discharges.

$$u_{i+\Delta t}^2 = 2gx\tan\theta_b \tag{9}$$

It is illustrated in Figure 9 that for ideal non-erodible dams (depicted as dam A), the shear stress τ_b linearly increases along the x-direction (Figure 9, line A) resulting from the steady increase of u_i downstream. Observations from

21699011, 2022, 10, Downloaded from https://agupubs.onlinelibrary.wiley.com/doi/10.1029/2022JF006664 by Helmholtz-Zentrum Potsdam GFZ, Wiley Online Library on [21/11/2022]. See the Terms and Conditions (https://onlinelibrary.wiley.com/terms-and-conditions) on Wiley Online Library for rules of use; OA articles are governed by the applicable Creative Commons License

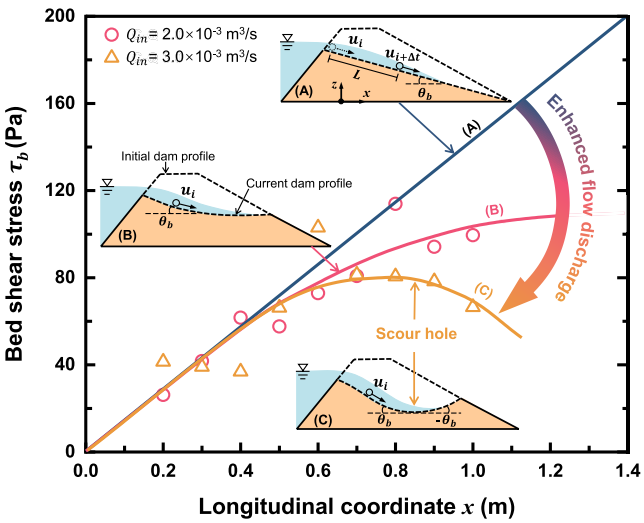

Figure 9. The change of the bed shear stress τ_b along the flow direction. The schematic diagrams of dams are qualitative illustrations of different shear stress distributions for different inflow discharges. The inverted triangle represents the water table behind the landslide dam; the blue and orange colors in the schematic diagram represent the dammed water and modeled landslide dam respectively; the dotted lines are the initial and current dam surface profiles. The blue line indicates an ideal condition (dam A), where τ_b varies linearly along the flow direction (hypothetical case). Pink and orange data points are τ_b for different inflow discharges Q_{in}. The scouring that result from these Q_{in} are depicted as dams B and C, respectively. The solid lines are guides to the eye and simply show the direction of the data trends.

the dam failures here at low inflow discharge reveal that the failure profiles are curved due to the influence of erosional features such as scour holes (dam B). Data points corresponding to shear stresses are measured from the experimental dams. In such cases, θ_b is minimal at the lowest point of the curvature on the dam surface resulting in weaker incoming flows with reduced erosive power. The slope of τ_b is thus reduced but still positive, as depicted by line B. At higher inflow/breach discharges, the scour holes become more evident (dam C) and change the channel surface gradients, wherein θ_b may become negative (inclining upwards). The negative inclination further reduces u_i, leading to a dramatic decrease in τ_b (depicted as the decrease in the trend of line C in Figure 9). Therefore, the non-uniform distribution of the erosion rates is due to the irregular change of τ_b (increases first and then decreases) caused by the feedback between the channel surface gradients and the flow velocities. However, the analysis above pertaining to the formation of the positive feedback is fundamentally based on the existence of curved surface profiles that are observed from experiments, and cannot explain the mechanisms that control the initiation of these erosional features.

3.3. Numerical Results

Based on our experimental observations, the landslide dam failure process can be simplified as the erosion of steep channel beds inclined at angles larger than that of the receiving rivers (Rosgen, 1994). During dam breaching, sediment erosion, entrainment, and channel bed collapse (see Section 3.1) control the surface evolution during failure. Schematic diagrams of these processes for a unit area are depicted in Figure 10. Here we simulate the evolution of the dam surface profiles at the axis of symmetry by modeling the abovementioned processes using the numerical framework presented in Section 2.3.

As expressed in Equation 4, erosion is defined as the change in elevation of the dam surface h_s when the shear exerted by the overtopping flood τ_b exceeds the local apparent erosion resistance τ_{cb} (Figure 10a). In the model we only consider the erosion along the bed since bed erosion is found to be 2–3 times larger than sidewall erosion (Figure 8). The coefficient K_{db} is obtained from the mean value in Figure 7a while the linear equation in Figure 7b

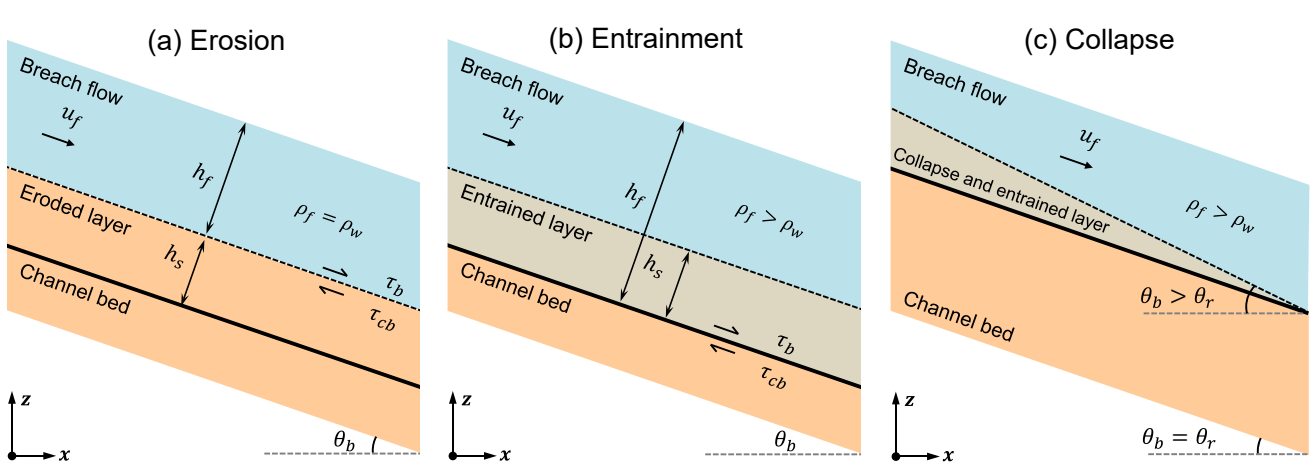

Figure 10. Schematic diagram of a two-layer model of a fluid flow interacting with an erodible bed capturing the (a) erosion, (b) entrainment, and (c) channel bed collapse for a unit calculation region. The u_f is the flow velocity, h_f is flow height, h_s is erosion depth, ρ_f and ρ_w are the flow density and pure water density, respectively. τ_b and τ_{cb} are the bed shear stress and apparent erosion resistance, respectively, θ_b is the inclination of channel bed while θ_r is the repose angle of bed materials. (a) Erosion occurs when τ_b is greater than τ_{cb}. (b) When this condition is satisfied, a soil layer of thickness h_s is added to the flood height h_f in the process of entrainment. The entrained sediment increases the density of the flood to be greater than that of water, that is, $\rho_f > \rho_w$. (c) Channel bed collapse occurs when the inclination of the channel bed is greater than the repose angle of the bed materials. At this time, the area labeled "collapse and entrained layer" is incorporated into the breach flow until $\theta_b = \theta_r$.

21699011, 2022, 10, Downloaded from https://agupubs.onlinelibrary.wiley.com/doi/10.1029/2022JF006664 by Helmholtz-Zentrum Potsdam GFZ, Wiley Online Library on [21/11/2022]. See the Terms and Conditions (https://onlinelibrary.wiley.com/terms-and-conditions) on Wiley Online Library for rules of use; OA articles are governed by the applicable Creative Commons License

is used to obtain τ_{cb}. The eroded sediment mass is entrained by the flow, contributing to the increase of its volumetric sediment concentration C_s and bulk density ρ_f (Figure 10b). Channel bed collapse occurs when the local bed inclination θ_b is larger than the repose angle of the dam materials θ_r. The sediment mass belonging to sections where $\theta_b > \theta_r$ are also entrained into the mixture flow (Figure 10c). Soils from slides and collapses along the sidewalls, that is, breach channel bank collapse (Zhong et al., 2018), are ignored in the calculations. All of these processes are implemented at every computational time step.

Dam failure profiles are obtained at four different dimensionless timesteps $t_* = t/t_b$ where t_b is the time when the breaching flow reaches the flume bed through the lowest point of the scour hole. This timescale is selected as a scaling parameter since beyond this time scour holes cease to develop. Figure 11 shows that the observed and simulated dam failure profiles are highly consistent at different t_*. It is noteworthy, that the model captures the development of scour holes at approximately the same location observed in the experiments. There is, however, a time difference between the dam breaching durations of the numerical simulations ($t_b = 46$ s) and the experimental ($t_b = 42$ s) tests. This may be because the model does not capture the random collapses in the lateral directions which also promote faster erosion. It is also possible that the small non-uniformities in the dam surface after the weak erosion stage (Stage 1 in Figure 4) induce positive erosion feedbacks (see Section 3.2.3) which may also accelerate the erosion process. Nevertheless, the numerical model here can adequately capture the breach morphology evolution during landslide dam failure and the dominant mechanisms that control it.

Different from our experimental setup, simulations are conducted only on the lower triangular area of the dam (inset of Figure 11b) since the upper dashed region in the inset of Figure 11b is eroded under weak flow conditions and is thus unstable. We are only interested in the stages when rapid erosion happens (Stages 2 and 3). Initially, the dam breach profile is assumed to be linear to avoid positive feedback during simulations.

4. Discussion

The landslide dam failure process is complex, involving flow dynamics (Powledge et al., 1989), hydraulic jumps (Walder et al., 2015), rapid bed and sidewall erosion (Chang & Zhang, 2010), breach side-slope instabilities (Zhong et al., 2018), and mass failures. Here we show that these mechanisms can be adequately accounted for by a simplified numerical model which assumes that the dam failure process is primarily controlled by erosion, particle entrainment, and channel bed collapse. In this study, we only focus on the morphological evolution under steady flow conditions and study the intrinsic mechanisms underlying the development of dam surface profiles. Numerical modeling can provide insights into the erosion processes that cannot be directly observed in experiments (e.g., volumetric sediment concentration) and allow for the evaluation of variables that are otherwise difficult to control (e.g., apparent erosion resistance). This allows us to elucidate the underlying mechanisms and factors that control the nonlinear erosional features during landslide dam breaching.

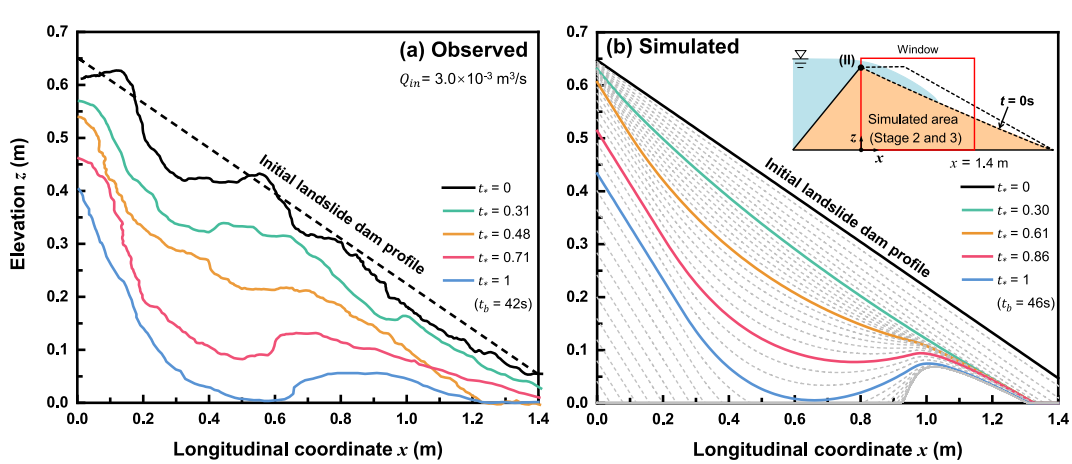

Figure 11. Comparison of longitudinal profiles obtained in the (a) experiments and (b) simulations. Dam profiles are obtained at different dimensionless failure times $t_* = t/t_b$, where t_b is the total time when the water flow reaches the flume bed (the dashed gray lines in panel (b) are erosion surface profiles between the selected times).

21699011, 2022, 10, Downloaded from https://agupubs.onlinelibrary.wiley.com/doi/10.1029/2022JF006664 by Helmholtz-Zentrum Potsdam GFZ, Wiley Online Library on [21/11/2022]. See the Terms and Conditions (https://onlinelibrary.wiley.com/terms-and-conditions) on Wiley Online Library for rules of use; OA articles are governed by the applicable Creative Commons License

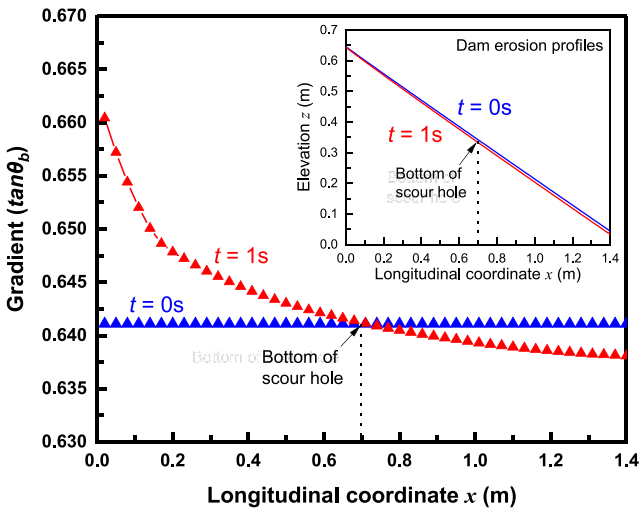

Figure 12. The gradients along the dam erosion surface at the initial time step and 1 s afterward. The inset shows dam surface profiles at different times derived from numerical simulations. The intersection of two lines at 0.7 m represents the bottom of scour hole.

4.1. The Formation of Scour Holes

In Section 3.2.3, we have shown that the emergence of nonlinear erosional features (i.e., scour holes) influence erosion at the dam surface. Here, we explain the mechanisms behind its formation through results obtained from the simulations. Figure 12 shows the longitudinal variation of gradients of the erosion surface along the flow direction at $t = 0$ s (blue markers) and another obtained 1 s later (red markers). The intersection of the two lines indicates the bottom of the scour hole at this time step. The inset shows the corresponding dam erosion profiles demonstrating that the scour hole forms at the very beginning of the dam breaching. This phenomenon can be partly explained in terms of the theory proposed by Parker and Izumi (2000) and Izumi and Parker (2000) on the emergence of cyclic step pools wherein the scour hole here can be assumed to be a solitary step. They explained that as the fluid makes its way downslope over a cohesive erodible surface, it entrains the bed sediment. The flow is initially slow-moving (in the sub-critical regime with respect to the Froude number), but at the same time inhibits deposition. Further downstream, the flow increases in velocity (moving toward the supercritical regime) up until it achieves a limiting velocity. This velocity is referred to as a hydraulic jump condition which corresponding to a threshold shear stress over which flow energy is abruptly dissipated. In such a case, further erosion is inhibited and the change in the surface gradient due to erosion is decreased. The bottom of the scour hole is the point at which this limiting velocity is achieved. Indeed, as shown in Figure 8, the increased velocity induces greater shear stress which results in more erosion. The hydraulic jump condition that controls the scouring at the initial step in their model, however, is not easy to define in this study. In the absence of irregularities in the erodibility and profile of the dam surface, the velocity and erosive capacity of the flow will ideally proceed unimpeded and will thus result in a linear surface profile (i.e., no scour hole). Hence, it is reasonable to assume that for a dam composed of homogenous soil, changes in the shear stress result from changes in the properties of the eroding flood. In the following section, we show that the limiting condition which results in stronger erosion at the bottom of the scour hole is instead related to the increase in the apparent erosion resistance τ_c (Figure 7b).

4.2. The Influence of Apparent Erosion Resistance on Scour Hole Formation

To further explore the factors controlling of scour holes, additional simulations are implemented to investigate the influence of dam material parameters, and the processes of erosion, entrainment, and collapse on the dam failure profiles. Model settings are summarized in Table 2, and the corresponding flow velocity (i.e., the t_* from 0 to 1) and longitudinal dam profiles are illustrated in Figure 13. Test case No. 1 (Figures 13a and 13b) considers all three possible processes involved in dam breaching and acts as a reference case. It should be noticed that flow velocity and dam profiles vary significantly with time because of the feedback mechanisms detailed in the previous sections. Test case No. 2 (Figures 13c and 13d) shows that although varying K_d results to slight variations in flow velocity and dam surface profiles, the non-uniform distribution of erosion rates and scour holes are still observed.

Figures 13e and 13g show that scour holes still form even when entrainment and dam collapse processes are not considered, whereas Figure 13i shows that scour holes develop sharply when only erosion is considered. Note that when entrainment is ignored, the sediment mass that is displaced due to erosion is not incorporated into the overtopping flow in such a way that the ρ_f equals to ρ_w at all times. The non-consideration of sediment entrainment confines erosion at the upper sections of the dam (near the dam crest) which then quickly weakens toward the lower portions where τ_c is increasing (Figure 13f). Ignoring dam surface collapses results in very steep surface gradients near the breach section O (Figures 13h and 13j), which is inconsistent with what is observed in the experimental profiles. We further test the sensitivity of the dam profile evolution on the apparent erosion resistance (τ_c) in Figures 13k and 13l wherein it is shown that no scour hole develops when τ_c is kept constant along the dam surface, and the velocity profiles do not significantly change with time. This behavior is consistent throughout different values of τ_c (i.e., τ_c =10 and 30 Pa, but not shown in Figure 13l). This illustrates that the

21699011, 2022, 10, Downloaded from https://agupubs.onlinelibrary.wiley.com/doi/10.1029/2022JF006664 by Helmholtz-Zentrum Potsdam GFZ, Wiley Online Library on [21/11/2022]. See the Terms and Conditions (https://onlinelibrary.wiley.com/terms-and-conditions) on Wiley Online Library for rules of use; OA articles are governed by the applicable Creative Commons License

Table 2
List of Numerical Input Parameters for Different Simulation Scenarios

Test ID	Erosion	Entrainment	Collapse	Erodibility K_d (mm/Pa-s)	Apparent erosion resistance τ_c (Pa)
*No. 1	Yes	Yes	Yes	0.59	$\tau_c = 57.36x + 0.25$
No. 2	Yes	Yes	Yes	**0.40**	
No. 3	Yes	No	Yes	0.59	
No. 4	Yes	Yes	**No**	0.59	
No. 5	Yes	**No**	**No**	0.59	
No. 6	Yes	Yes	Yes	0.59	$\boldsymbol{\tau_c = [10, 20, 30]}$

Note. Asterisk indicates the parameters that are identical to the experimental test $Q_{in} = 3.0 \times 10^{-3}$ m^3/s. The parameters in bold are those varied in the simulations.

increase in τ_c along the flow direction is necessary for the initiation and development of scour holes along the dam surface. These results show that although erosion controls the formation of scour holes, through the longitudinal increase of τ_c, sediment entrainment and channel bed collapse likewise affect the evolution of the landslide dam surface during failure.

4.3. The Influence of Volumetric Sediment Concentration on the Apparent Erosion Resistance

In this work, the apparent erosion resistance (τ_c) increases consistently along the flow direction (Figure 7b). Previous literature has shown that τ_c depends on the bed geometry (Turowski et al. (2011), physical properties of the bed sediment (e.g., particle size, moisture, compaction, soil shear strength, dispersion, and plasticity), chemical composition (Na, K, Ca, Mg content, and soil pH), meteorological (temperature and freeze-thaw), and biological conditions (plant roots) (Knapen et al., 2007). Other works have also shown that the properties of the overtopping flow, such as flow regimes, particle Reynolds number (Cheng, 2004; Dade et al., 1992; Paphitis, 2001), and sediment concentration (Buffington & Montgomery, 1997; G. G. D. Zhou et al., 2019; H. W. Zhang, 2012; Papa et al., 2004) may also affect τ_c. Papa et al. (2004) found that the capacity of the water flow to entrain particles on the channel bed depends on the sediment concentration. Zhang (2012) proposed that τ_c is proportional to a critical incipient velocity that is correlated to C_s for both cohesive and non cohesive soils. Figure 14 shows that sediment concentration increases along the flow direction up until it reaches a maximum value (saturation). The breach flow first entrains the channel bed sediments with an approximately constant slope from $x = 0$ to 0.4 m. The slope then starts to decrease continuously until the flow becomes saturated. The larger the slope, the easier it is for the flow to entrain more sediment particles. This result is consistent with the findings of Wang (1999) and Zhang (2012), who suggested that it is harder for turbid sediment-laden fluid to entrain more particles than it is for clear sediment-free flow. We also find that this gradual saturation of breach flow coincides with the region where the scour hole is located, suggesting a relation between scour hole formation and the sediment concentration. Since the formation of scour holes has been demonstrated to depend on the apparent erosion resistance (Figure 13), it is interesting to see whether τ_c also depends on C_s as suggested by Wang (1999) and Zhang (2012).

Figure 15 shows the relationship between dimensionless apparent erosion resistance versus sediment concentration from our simulations and from previous theoretical (H. W. Zhang, 2012) and experimental results (Papa et al., 2004). We find that τ_c exponentially increases with the entrained sediment concentration, which means that τ_c increases along the flow direction since the incoming flow is already gradually saturated with sediments due to erosion and entrainment. Figure 15c, compares our numerical results with the experimental trend of Papa et al. (2004), wherein our results are two orders of magnitude greater. This is probably due to the greater breach flow velocities, induced by higher inflow discharges and channel bed inclination used here, which in turn result in greater shear stresses (i.e., approximately 10 times greater). The apparent erosion resistance is also correspondingly greater since here it is not only a function of the dam surface material but of the outburst flood as well. Despite the difference in scale, the qualitative similarity in the trend of both data sets - a positive relationship between τ_c and C_s - is still evident. In the model of Zhang (2012), τ_c exhibits a weaker positive dependence on C_s (Figure 15a) probably because their model mainly accounts for the particle size distribution, grain protrusion of the channel bed, and the water flow temperature, thereby underestimating the influence of the sediment concentration on the apparent erosion resistance. Based on Equation 4, the erosion rate decreases with the increasing τ_c

21699011, 2022, 10, Downloaded from https://agupubs.onlinelibrary.wiley.com/doi/10.1029/2022JF006664 by Helmholtz-Zentrum Potsdam GFZ, Wiley Online Library on [21/11/2022]. See the Terms and Conditions (https://onlinelibrary.wiley.com/terms-and-conditions) on Wiley Online Library for rules of use; OA articles are governed by the applicable Creative Commons License

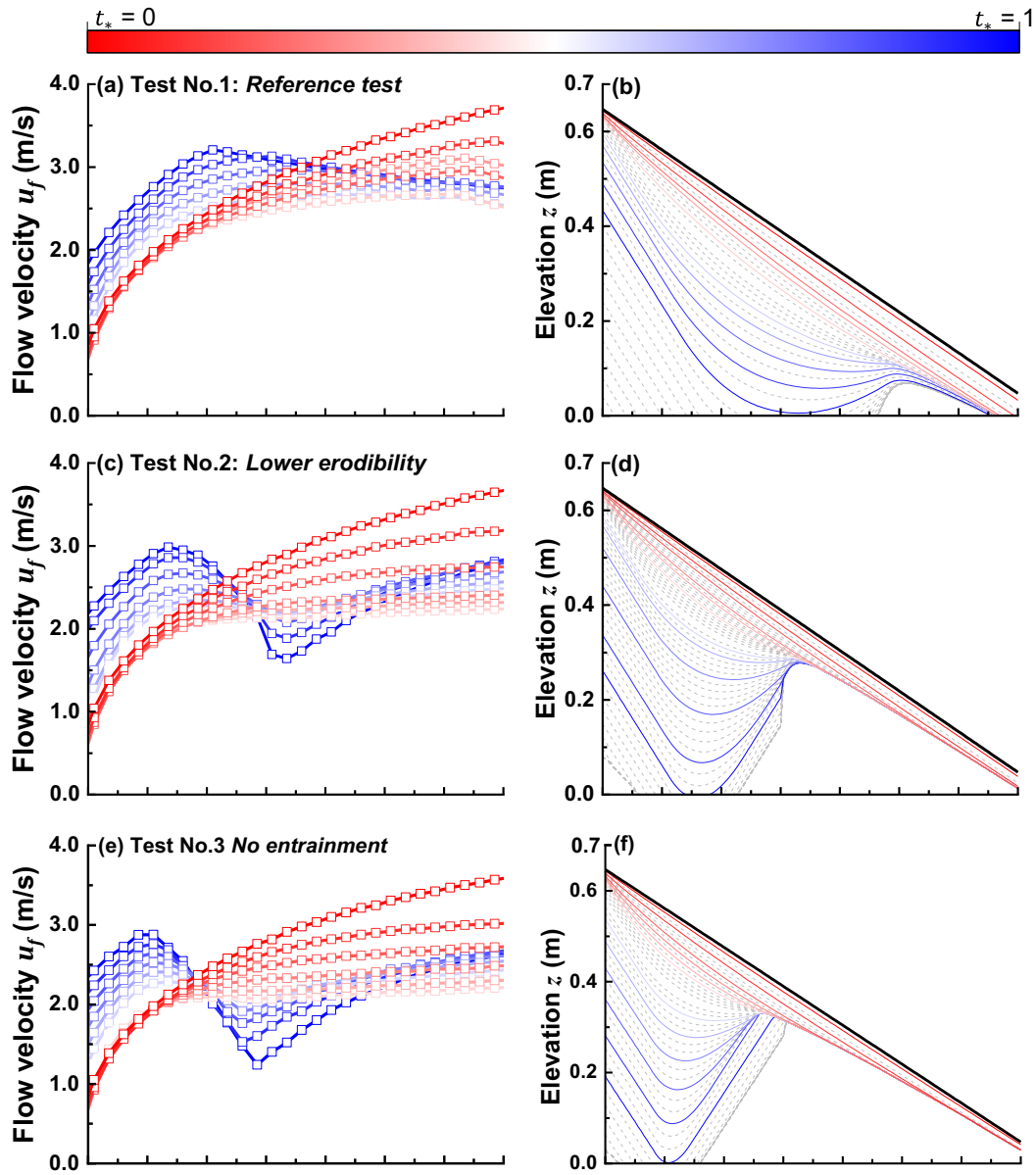

Figure 13. Model simulation results for the different test cases enumerated in Table 2 for an inflow discharge of 3.0×10^{-3} m^3/s. The gradual change in color represents the transition in time from the beginning of the dam breaching ($t_* = 0$) to the time at which the dam surface reaches the channel bed ($t_* = 1$). The left column is the temporal evolution of the flow velocity, which corresponds to the longitudinal erosion profiles (the dashed lines are the erosion surface profiles between selected times) in the right column. Note that each line in panels (k and l) still represents different points in time although no change in color is observed since no scour holes form.

and thus C_s. Our model considers the influence of sediment concentration (C_s) on bed erosion rate (E_b), which was not taken into account in most of the previous models (Table S4 in Supporting Information S1). Only few models have captured this negative relationship between erosion rate and sediment concentration (e.g., Pontillo et al., 2010; Takahashi, 1991).

To summarize, we find that the initial formation of scour holes on the surface of landslide dams during breaching results from the increase of the apparent erosion resistance along the dam surface. This apparent increase in erosion resistance is due to the gradual saturation of overtopping flow with entrained bed sediment. The saturation diminishes the capacity of the flow to entrain more dam material as it makes its way further downslope. The

21699011, 2022, 10, Downloaded from https://agupubs.onlinelibrary.wiley.com/doi/10.1029/2022JF006664 by Helmholtz-Zentrum Potsdam GFZ, Wiley Online Library on [21/11/2022]. See the Terms and Conditions (https://onlinelibrary.wiley.com/terms-and-conditions) on Wiley Online Library for rules of use; OA articles are governed by the applicable Creative Commons License

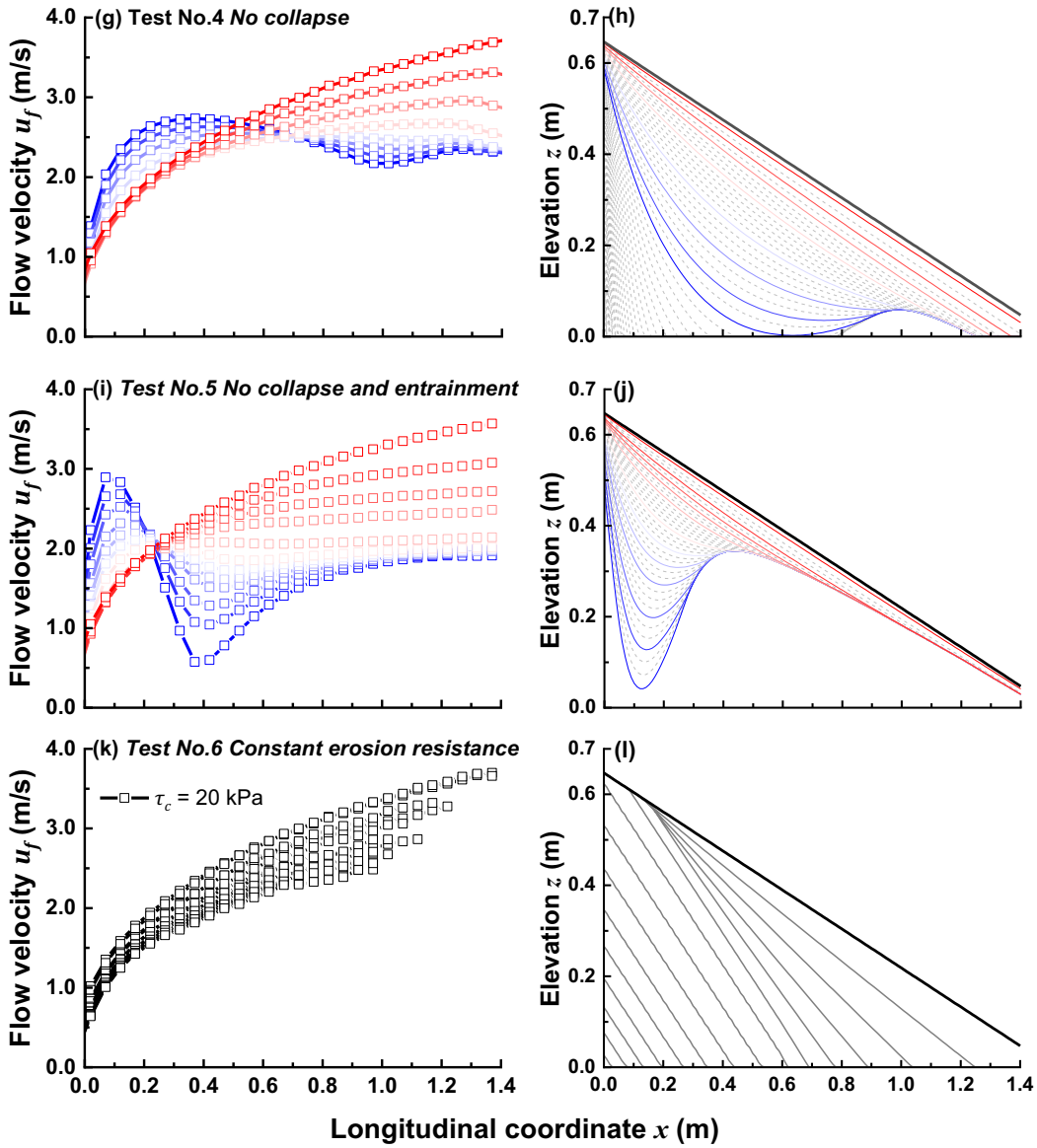

Figure 13. (Continued)

initial formation of this erosional feature will further lead to localized changes in the flow velocity, and hence flow shear stress, which in turn will promote greater scouring.

4.4. Implications for Landslide Dam Modeling

The sudden drainage of lakes due to the failure of landslide dams may induce catastrophic outburst floods (House et al., 2002; P. Cui et al., 2012) that can rework valley floors (Cook et al., 2018; Delaney & Evans, 2015; Turzewski et al., 2019). The magnitudes and temporal evolution of these floods are influenced by the erosion of the dam surface by the breaching flood. Hence the accurate definition of the erosion process and its underlying mechanisms are necessary for the prediction of outburst flood hydrographs. A conceptual diagram of how erosion shapes the failure profile of landslide dams, derived from the results of this work, is presented in Figure 16. The distribution of erosion rates at different streamwise locations of the landslide dam surface varies non-uniformly, evidenced by the formation of erosional features such as scour holes. Although scour holes during dam breaching have not yet been observed in nature, they have been reported in experimental landslide dams having different

21699011, 2022, 10, Downloaded from https://agupubs.onlinelibrary.wiley.com/doi/10.1029/2022JF006664 by Helmholtz-Zentrum Potsdam GFZ, Wiley Online Library on [21/11/2022]. See the Terms and Conditions (https://onlinelibrary.wiley.com/terms-and-conditions) on Wiley Online Library for rules of use; OA articles are governed by the applicable Creative Commons License

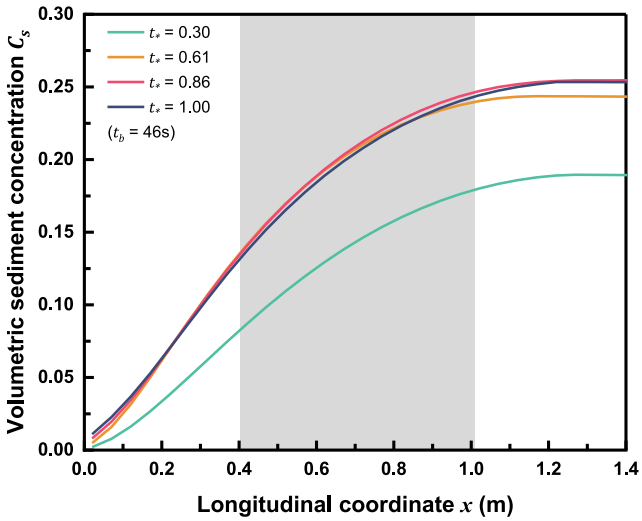

Figure 14. The volumetric sediment concentration along the flow direction at dimensionless times corresponds to those in Figure 11b. The shaded area represents the location of the final scour hole in Figure 11b.

sizes and material compositions (Do et al., 2016; Niu et al., 2012; Zhong et al., 2019). This hints that this feature may also occur in natural landslide dams but remains undetected largely due to difficulties in observing landslide dam breaching in the field. The formation of these surface features results from the difference in the shear stress exerted by the breach flood on the dam surface and the resistance of the bed sediment to shear. Initially, as the flow proceeds further downstream it carries eroded sediments, becoming increasingly saturated until such a point that it can no longer entrain more particles. This is manifested as an apparent linear increase in erosion resistance quantified by τ_{cb}. This means that the apparent resistance is not necessarily an inherent property of the dam surface material but is also controlled by the capacity of the overtopping flood to entrain bed material. This results in the non-uniform entrainment of dam surface sediment wherein fewer sediments are carried near the dam toe relative to the upper regions, later leading to the observed scour holes. The curved surface profile influences flood velocity, and hence the flow shear stress τ_b, in such a way that erosion weakens near the base of the scour holes.

Results from our numerical model further reveal a fundamental correlation between the erosion mechanisms and breach morphology evolution during landslide dam breaching. This information can be useful for developing more accurate physical-based outburst flooding models as well as means to accurately measure processes in the field to validate these models. Results here can also be used to develop three-dimensional landslide dam erosion models in the future. Specifically, accounting for the erosion, entrainment, and mass collapse of dam sections is expected to enhance the predictive capabilities of landslide dam failure models as demonstrated in Figure 11. Results here also provide insight into the geomorphic changes in channel systems affected by dam breaching floods which may improve long-term landscape evolution models. Our

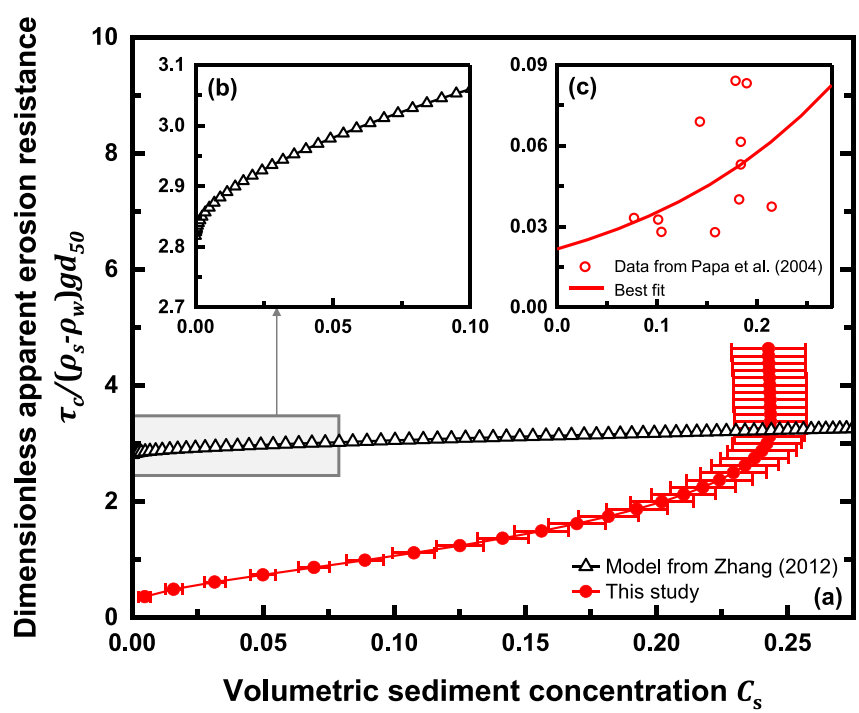

Figure 15. The relationship between dimensionless apparent erosion resistance and volumetric sediment concentration obtained (a) from our simulation results, (b) from the model of Zhang (2012), and (c) from the experimental results of Papa et al. (2004). The empty circles in panel (c) are the experimental data points from Papa et al. (2004) while the red solid line is the best fit line. Error bars for sediment concentration express the standard deviations.

21699011, 2022, 10, Downloaded from https://agupubs.onlinelibrary.wiley.com/doi/10.1029/2022JF006664 by Helmholtz-Zentrum Potsdam GFZ, Wiley Online Library on [21/11/2022]. See the Terms and Conditions (https://onlinelibrary.wiley.com/terms-and-conditions) on Wiley Online Library for rules of use; OA articles are governed by the applicable Creative Commons License

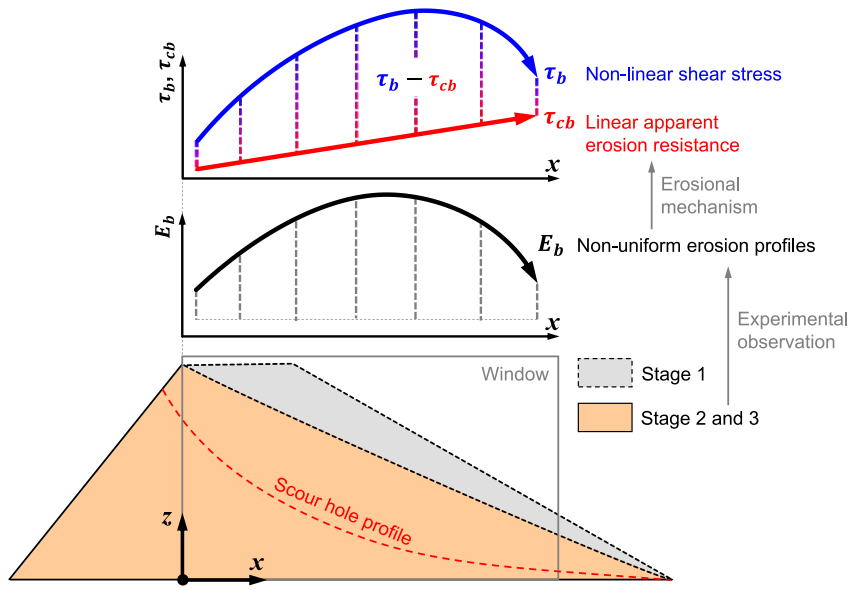

Figure 16. A conceptual diagram defining the formation of non-uniform erosional surface features during the landslide dam breaching.

results can be beneficial in quantifying the potential for erodibilities and studying the channel evolution during outburst floods in different drainage network portions during dam breaching and outburst flooding processes.

4.5. Limitations

The geotechnical characterization of landslide dams is closely related to the GSD of the materials that they are made of (Casagli et al., 2003). Dam materials and their size distributions may significantly vary depending on the process which led to their formation, for example, large rockslides, volcanic mass movements, debris flows, etc. (Hungr et al., 2014; X. M. Fan et al., 2020). To replicate real landslide dams, the model dams in this study use material obtained from the debris flow alluvial fan and are constructed following identical geometrical conditions. However, a common limitation in landslide dam experiments is that they cannot reproduce the actual damming or river blocking mechanisms that occur in nature (X. Fan et al., 2021; X. M. Fan et al., 2020). Idealized dams here are representative only of those formed by slides or flows of unconsolidated sediments which make up only a fraction of landslide dam cases occurring globally. In addition, in laboratory-scale studies, water only interacts with the dam after it has been constructed whereas in nature landslide materials are pushed into flowing rivers. The interactions that occur during this transient process may also affect the consolidation of the dam materials and their subsequent failure. Nevertheless, the mechanisms of dam surface evolution presented here largely depend on the interactions between the surface sediment and the overtopping fluid, and are expected to hold true in situations where particle sizes within the bulk do not dramatically vary so as to affect the local erodibility of the dam surface.

Processes that occur during material transport, such as particle size segregation (C. G. Johnson et al., 2012; K. F. E. Cui et al., 2021), may result in grain sorting in deposits and features such as carapaces (X. Fan et al., 2021). These features lead to heterogeneities in the dam's internal structure that may influence the dam's stability and the erosion mechanisms during breaching. Inhomogeneities in the grain size and degree of consolidation along the dam height may also affect the erodibility of the dam surface. Indeed, the mechanisms presented here that control the formation of scour holes largely assume that the surface erodibility is uniform at different locations and only the apparent erosion resistance varies (due to the gradual saturation of the overtopping flow with sediment) in the modeling process. In this work, we are only interested in the influence of different hydrological factors on the surface evolution of landslide dams during breaching and for simplicity, the effects of grain sorting and stratigraphy are isolated by evenly distributing the component particle sizes within the dam body and preparing the dam under uniform compaction. A dedicated investigation of the influence of sedimentology on surface erosion in landslide dams is consigned to future work.

21699011, 2022, 10, Downloaded from https://agupubs.onlinelibrary.wiley.com/doi/10.1029/2022JF006664 by Helmholtz-Zentrum Potsdam GFZ, Wiley Online Library on [21/11/2022]. See the Terms and Conditions (https://onlinelibrary.wiley.com/terms-and-conditions) on Wiley Online Library for rules of use; OA articles are governed by the applicable Creative Commons License

In this study, we only focus on erosion processes without any deposition. We minimize the random deposition at the dam toe and channel bed downstream in the experimental setup by using an angle of inclination that is larger relative to those observed in natural river beds in mountainous areas. This inhibits deposition by allowing the material to be easily washed away by the breach flood. However, it should be noted that the expanded breach channels due to erosion further increase the inflow discharge and may result in the collapse of unstable sections of the dam. These collapsed materials locally block the channel, forming knick-points which may also result in local negative θ_b (Figure 9) that can further slow the flow down dramatically. This causes a dramatic decrease in τ_b and promotes the formation of scour holes during breaching. The systematic consideration of the deposition during landslide dam failure is consigned to future research.

In addition, we only use the dominant bed erosion to explore the controls of non-uniform erosional features and ignore the effects of sidewall erosion on the evolution of the channel bed. Even though the simulations show a good agreement with the observed erosion profiles, the specific effects of sidewall erosion on the channel bed evolution remain to be investigated.

5. Concluding Remarks

The failure of landslide dams is an erosion-driven process along the vertical and lateral directions. In this study, we elucidate the relationships between key hydraulic parameters and the breach morphology evolution during the overtopping failure of landslide dams through flume experiments and numerical simulations. We show here that the breaching process can be divided into three stages, where each stage is characterized by distinct levels of breach discharge and stream power. The breach discharge in the first stage is weak, and the erosive capacity of the overtopping flow is low. Erosion increases rapidly and is found to be strongest in the second stage. As the impounded fluid behind the dam is diminished and the breach size ceases to increase, the flood slows down and the erosive power weakens in the third stage. During the entire dam breaching, the erosion rates on the channel bed are greater than the erosion at the sidewalls.

The analysis of mechanisms that control dam surface evolution is conducted when the erosion is most rapid. Measurements of flow properties at different sections along the dam surface show that the difference between the flow shear stress and the apparent erosion resistance along the dam surface controls the erosion rates in both vertical and lateral directions. The shear stress, in both directions, increases before decreasing after exceeding a peak value while the apparent erosion resistance linearly increases with the longitudinal distance. This results in the formation of scour holes.

Based on observations from the experiments, a depth-averaged numerical model which accounts for the erosion, entrainment, and channel bed collapse is used to model dam surface evolution during failure. This model incorporates the constant erodibility and linear increase of the erosion resistance obtained from the experiments. Good agreement is obtained between the simulation results and the measured dam profiles. Simulations further show that the initial development of erosional features such as scour holes is strongly dependent on the increasing apparent erosion resistance of the overtopping flow. Simulations, where the erosion resistance is assumed to be constant along the dam surface, do not result in scour holes. The apparent erosion resistance is not only a property of the dam surface but also of the water flow moving downslope. As soil particles are eroded and entrained into the flow, it becomes gradually saturated with sediment, and its ability to erode and transport sediment decreases. The point at which the limit sediment concentration is achieved determines the lower boundary of the scour hole. These localized erosional features induce changes in the local flow velocities, and shear stresses, which in turn further promote its development.

Our work attempts to understand the mechanisms that control the breach morphology evolution of landslide dams during breaching. A new perspective on the dam erosion process and its relationship with the sediment concentration and the apparent erosion resistance is presented and demonstrated here, making it possible to provide more accurate physically based outburst flood predictions. For future work, it will be beneficial to consider the effects of sedimentary sequences and stratigraphy on dam breaching.

Notations

C_s	Volumetric sediment concentration
d_{50}	Mean diameter of the model dam materials

21699011, 2022, 10, Downloaded from https://agupubs.onlinelibrary.wiley.com/doi/10.1029/2022JF006664 by Helmholtz-Zentrum Potsdam GFZ, Wiley Online Library on [21/11/2022]. See the Terms and Conditions (https://onlinelibrary.wiley.com/terms-and-conditions) on Wiley Online Library for rules of use; OA articles are governed by the applicable Creative Commons License

E_b, E_w	Bed erosion rate; sidewall erosion rate
f_i	Body force
f_{bs}	Basal frictional resistance calculated from Manning's formula
g	Acceleration due to gravity
GSD	Grain size distribution
H_d	Height of the landslide dam
h_f, h_s	Depth of water flow; erosion depth at a certain section or location
k_{ap}	Lateral earth pressure coefficient
K_d, K_{db}, K_{dw}	Erodibility of dam materials; erodibility of channel bed materials; and erodibility of sidewalls materials
L, L_d	Tracer particle travel distance; toe to toe dam length
n	Manning coefficient
p	Bed porosity
P	Normal component
Q_b, Q_{in}, Q_{out}	Breach discharge; inflow discharge; and outburst discharge
Q_{ib}, Q_{iout}	The inflection point of the hydrographs for the breach discharge and outburst discharge, respectively
Q_{pb}, Q_{pout}	Peak discharge of the hydrographs for the breach discharge and outburst discharge respectively
R^2	Goodness of fit
$RMSE$	Root Mean Squared Error
t_0, t_b, t_p, t_*	The initial time of the overtopping; the total time when the water flow reached the flume bed; the time to peak discharge; dimensionless timesteps
$\boldsymbol{T}$	Stress tensor
$\boldsymbol{I}$	Unit tensor
u_f	Flow velocity
u_i	The velocity of a tracer particle at any time step i
$\boldsymbol{u}$	Flow velocity vector
V_l, V_d	The volume of the dammed lake and model dams
W_{btop}, $W_b, \tilde{W}_b$	The top width of the channel breach; width of the breach; and the arch length of the breach crest
w_b	Channel width at different locations (sections)
x, y, z	Coordinate of downstream flow direction, lateral direction, and perpendicular to flow direction x and lateral direction y
$\overline{\alpha}$	Mean value of the parabola coefficient
γ	The ratio between the surface velocity and the mean velocity
ε	Coefficient between mean bed shear stress and sidewall shear stress
$\theta_1, \theta_2, \theta_3, \theta_b, \theta_r$	The angle of dam toe upstream and downstream; the ambient slope of the river bed; the inclination of erodible channel bed; and repose angle of soils
μ_k	Dynamic friction factor
ρ_w, ρ_f, ρ_s	The density of water flow (1,000 kg/m^3); the density of flood; and the density of soils (2,650 kg/m^3)
τ, τ_b, τ_w	Shear stress exerted by the water flow on the channel bed and sidewalls
$\tau_c, \tau_{cb}, \tau_{cw}$	Apparent sediment erosion resistance; apparent sediment erosion resistance of the channel bed and sidewalls
Ω	Stream power at the breach section
(I)	Dam shoulder section downstream
(II)	Dam shoulder section upstream
i	represents different time steps
j	represents different sections
Δ_x, Δ_y	The distance along the x and y directions in a certain period for tracer particle
$\Delta m, \Delta M$	Rate of mass change of the overtopping flow; flow momentum change
$\Delta E\%$	The percentage difference between measured and calculated quantities

21699011, 2022, 10, Downloaded from https://agupubs.onlinelibrary.wiley.com/doi/10.1029/2022JF006664 by Helmholtz-Zentrum Potsdam GFZ, Wiley Online Library on [21/11/2022]. See the Terms and Conditions (https://onlinelibrary.wiley.com/terms-and-conditions) on Wiley Online Library for rules of use; OA articles are governed by the applicable Creative Commons License

Data Availability Statement

Figures were made with OriginPro (2022) version 2022b Education Edition (OriginLab), available under the OriginLab license at https://www.originlab.com/. Data that can be used to replicate and validate the results presented here, including experimental measurements and simulation outputs, are available at Zenodo via: G. G. D. Zhou et al. (2022) (https://doi.org/10.5281/zenodo.7050542).

Acknowledgments
The authors appreciate Mingjun Zhou for providing support in conducting the experiments. The authors would also like to thank the Editor Amy East, the Associate Editor Oliver Korup, the reviewer Anne-Laure Argentin and other anonymous reviewers whose comments and suggestions greatly improved this work. The authors acknowledge the financial support from the National Natural Science Foundation of China (Grant Nos. 41941017 and 41731283), the Key Collaborative Research Program of the Alliance of International Science Organizations (Grant No. ANSO-CR-KP-2021-07), and the Chinese Academy of Sciences (CAS) "Light of West China" Program, and Sino-German Mobility Program (Grant No. M-0145).

References

Annandale, G. W. (2006). *Scour technology: Mechanics and engineering practice*. McGraw-Hill. https://doi.org/10.1036/0071440577

Argentin, A.-L., Robl, J., Prasicek, G., Hergarten, S., Hölbling, D., Abad, L., & Dabiri, Z. (2021). Controls on the formation and size of potential landslide dams and dammed lakes in the Austrian Alps. *Natural Hazards and Earth System Sciences*, *21*(5), 1615–1637. https://doi.org/10.5194/nhess-21-1615-2021

Bagnold, R. A. (1966). *An approach to the sediment transport problem from general physics*. US Government Printing Office. https://doi.org/10.3133/pp422I

Balmforth, N. J., von Hardenberg, J., Provenzale, A., & Zammett, R. (2008). Dam breaking by wave-induced erosional incision. *Journal of Geophysical Research*, *113*(F1), F01020. https://doi.org/10.1029/2007JF000756

Bruce, P. C., Shmueli, G., & Patel, N. R. (2016). *Data mining for business analytics: Concepts, techniques, and applications with XLMiner*. John Wiley & Sons.

Brunner, M. I., Gilleland, E., Wood, A., Swain, D. L., & Clark, M. (2020). Spatial dependence of floods shaped by spatiotemporal variations in meteorological and land-surface processes. *Geophysical Research Letters*, *47*(13), e2020GL088000. https://doi.org/10.1029/2020GL088000

Buffington, J. M., & Montgomery, D. R. (1997). A systematic analysis of eight decades of incipient motion studies, with special reference to gravel-bedded rivers. *Water Resources Research*, *33*(8), 1993–2029. https://doi.org/10.1029/96WR03190

Cantero-Chinchilla, F. N., Castro-Orgaz, O., Dey, S., & Ayuso-Muñoz, J. L. (2016). Nonhydrostatic dam break flows. II: One-dimensional depth-averaged modeling for movable bed flows. *Journal of Hydraulic Engineering*, *142*(12), 04016069. https://doi.org/10.1061/(ASCE)HY.1943-7900.0001206

Casagli, N., Ermini, L., & Rosati, G. (2003). Determining grain size distribution of the material composing landslide dams in the Northern Apennines: Sampling and processing methods. *Engineering Geology*, *69*(1–2), 83–97. https://doi.org/10.1016/S0013-7952(02)00249-1

Castro-Orgaz, O., Hager, W. H., & Cantero-Chinchilla, F. N. (2022). Shallow flows over curved beds: Application of the Serre-Green-Naghdi theory to weir flow. *Journal of Hydraulic Engineering*, *148*(1), 04021053. https://doi.org/10.1061/(asce)hy.1943-7900.0001954

Cenderelli, D. A., & Wohl, E. E. (2001). Peak discharge estimates of glacial-lake outburst floods and "normal" climatic floods in the Mount Everest region, Nepal. *Geomorphology*, *40*(1–2), 57–90. https://doi.org/10.1016/S0169-555X(01)00037-X

Chang, D. S., & Zhang, L. M. (2010). Simulation of the erosion process of landslide dams due to overtopping considering variations in soil erodibility along depth. *Natural Hazards and Earth System Sciences*, *10*(4), 933–946. https://doi.org/10.5194/nhess-10-933-2010

Chanson, H. (2004). *Hydraulics of open channel flow*. Elsevier. https://doi.org/10.1016/B978-0-7506-5978-9.X5000-4

Chen, D., Wang, Y., Melville, B., Huang, H., & Zhang, W. (2018). Unified formula for critical shear stress for erosion of sand, mud, and sand–mud mixtures. *Journal of Hydraulic Engineering*, *144*(8), 04018046. https://doi.org/10.1061/(ASCE)HY.1943-7900.0001489

Chen, Z. Y., Ma, L. Q., Shu, Y., Chen, S. J., Xu, L., Sun, P., & Li, X. (2015). Back analysis of the draining process of the Tangjiashan barrier lake. *Journal of Hydraulic Engineering*, *141*(4), 05014011. https://doi.org/10.1061/(ASCE)HY.1943-7900.0000965

Cheng, N.-S. (2004). Analysis of bedload transport in laminar flows. *Advances in Water Resources*, *27*(9), 937–942. https://doi.org/10.1016/j.advwatres.2004.05.010

Chepil, W. (1959). Equilibrium of soil grains at the threshold of movement by wind. *Soil Science Society of America Journal*, *23*(6), 422–428. https://doi.org/10.2136/sssaj1959.03615995002300060019x

Coleman, S. E., Andrews, D. P., & Webby, M. G. (2002). Overtopping breaching of noncohesive homogeneous embankments. *Journal of Hydraulic Engineering*, *128*(9), 829–838. https://doi.org/10.1061/(ASCE)0733-9429(2002)128:9(829)

Cook, K. L., Andermann, C., Gimbert, F., Adhikari, B. R., & Hovius, N. (2018). Glacial lake outburst floods as drivers of fluvial erosion in the Himalaya. *Science*, *362*(6410), 53–57. https://doi.org/10.1126/science.aat4981

Costa, J. E., & Schuster, R. L. (1988). The formation and failure of natural dams. *The Geological Society of America Bulletin*, *100*(7), 1054–1068. https://doi.org/10.1130/0016-7606(1988)100<1054:TFAFON>2.3.CO;2

Cui, K. F. E., Zhou, G. G. D., & Jing, L. (2021). Viscous effects on the particle size segregation in geophysical mass flows: Insights from immersed granular shear flow simulations. *Journal of Geophysical Research: Solid Earth*, *126*(8), e2021JB022274. https://doi.org/10.1029/2021JB022274

Cui, P., Dang, C., Zhuang, J. Q., You, Y., Chen, X. Q., & Scott, K. M. (2012). Landslide-dammed lake at Tangjiashan, Sichuan province, China (triggered by the Wenchuan Earthquake, May 12, 2008): Risk assessment, mitigation strategy, and lessons learned. *Environmental Earth Sciences*, *65*(4), 1055–1065. https://doi.org/10.1007/s12665-010-0749-2

Cui, P., Zhu, Y. Y., Han, Y. S., Chen, X. Q., & Zhuang, J. Q. (2009). The 12 May Wenchuan earthquake-induced landslide lakes: Distribution and preliminary risk evaluation. *Landslides*, *6*(3), 209–223. https://doi.org/10.1007/s10346-009-0160-9

Dade, W., Nowell, A., & Jumars, P. (1992). Predicting erosion resistance of muds. *Marine Geology*, *105*(1–4), 285–297. https://doi.org/10.1016/0025-3227(92)90194-M

Davies, T., Manville, V., Kunz, M., & Donadini, L. (2007). Modeling landslide dambreak flood magnitudes: Case study. *Journal of Hydraulic Engineering*, *133*(7), 713–720. https://doi.org/10.1061/(ASCE)0733-9429(2007)133:7(713)

Dazzi, S., Vacondio, R., & Mignosa, P. (2019). Integration of a levee breach erosion model in a GPU-accelerated 2D shallow water equations code. *Water Resources Research*, *55*(1), 682–702. https://doi.org/10.1029/2018wr023826

Delaney, K. B., & Evans, S. G. (2015). The 2000 Yigong landslide (Tibetan Plateau), rockslide-dammed lake and outburst flood: Review, remote sensing analysis, and process modelling. *Geomorphology*, *246*, 377–393. https://doi.org/10.1016/j.geomorph.2015.06.020

Do, X. K., Kim, M., Nguyen, H. P. T., & Jung, K. (2016). Analysis of landslide dam failure caused by overtopping. *Procedia Engineering*, *154*, 990–994. https://doi.org/10.1016/j.proeng.2016.07.587

Ermini, L., & Casagli, N. (2003). Prediction of the behaviour of landslide dams using a geomorphological dimensionless index. *Earth Surface Processes and Landforms*, *28*(1), 31–47. https://doi.org/10.1002/esp.424

Fan, X., Dufresne, A., Whiteley, J., Yunus, A. P., Subramanian, S. S., Okeke, C. A. U., et al. (2021). Recent technological and methodological advances for the investigation of landslide dams. *Earth-Science Reviews*, *218*, 103646. https://doi.org/10.1016/j.earscirev.2021.103646

21699011, 2022, 10, Downloaded from https://agupubs.onlinelibrary.wiley.com/doi/10.1029/2022JF006664 by Helmholtz-Zentrum Potsdam GFZ, Wiley Online Library on [21/11/2022]. See the Terms and Conditions (https://onlinelibrary.wiley.com/terms-and-conditions) on Wiley Online Library for rules of use; OA articles are governed by the applicable Creative Commons License

Fan, X. M., Dufresne, A., Subramanian, S. S., Strom, A., Hermanns, R., Stefanelli, C. T., et al. (2020). The formation and impact of landslide dams – State of the art. *Earth-Science Reviews*, *203*, 103116. https://doi.org/10.1016/j.earscirev.2020.103116

Feliciano Cestero, J. A., Imran, J., & Chaudhry, M. H. (2015). Experimental investigation of the effects of soil properties on levee breach by overtopping. *Journal of Hydraulic Engineering*, *141*(4), 04014085. https://doi.org/10.1061/(ASCE)HY.1943-7900.0000964

Fraccarollo, L., & Capart, H. (2002). Riemann wave description of erosional dam-break flows. *Journal of Fluid Mechanics*, *461*, 183–228. https://doi.org/10.1017/s0022112002008455

Fread, D. L. (1988). *BREACH: An erosion model for earthen dam failures* (p. 35). Hydrologic Research Laboratory, National Weather Service, Office of Hydrology. Retrieved from http://rivermechanics.net/models/breach.pdf

Fujisawa, K., Kobayashi, A., & Yamamoto, K. (2008). Erosion rates of compacted soils for embankments. *Doboku Gakkai Ronbunshu C*, *64*(2), 403–410. https://doi.org/10.2208/jscejc.64.403

Garcia-Castellanos, D., & O'Connor, J. E. (2018). Outburst floods provide erodability estimates consistent with long-term landscape evolution. *Scientific Reports*, *8*(1), 10573. https://doi.org/10.1038/s41598-018-28981-y

Graf, W. H. (1984). *Hydraulics of sediment transport*. Water Resources Publications, LLC. Retrieved from https://books.google.com.hk/books?id=222b6L4WR-0C

Guo, Q.-C., & Jin, Y.-C. (1999). Modeling sediment transport using depth-averaged and moment equations. *Journal of Hydraulic Engineering*, *125*(12), 1262–1269. https://doi.org/10.1061/(ASCE)0733-9429(1999)125:12(1262)

Hager, W. H., & Schwalt, M. (1994). Broad-crested weir. *Journal of Irrigation and Drainage Engineering*, *120*(1), 13–26. https://doi.org/10.1061/(ASCE)0733-9437(1994)120:1(13)

Hakimzadeh, H., Nourani, V., & Amini, A. B. (2014). Genetic programming simulation of dam breach hydrograph and peak outflow discharge. *Journal of Hydrologic Engineering*, *19*(4), 757–768. https://doi.org/10.1061/(ASCE)HE.1943-5584.0000849

Hanson, G., Cook, K., & Hunt, S. (2005). Physical modeling of overtopping erosion and breach formation of cohesive embankments. *Transactions of the ASAE*, *48*(5), 1783–1794. https://doi.org/10.13031/2013.20012

Haschenburger, J. K., & Church, M. (1998). Bed material transport estimated from the virtual velocity of sediment. *Earth Surface Processes and Landforms*, *23*(9), 791–808. https://doi.org/10.1002/(SICI)1096-9837(199809)23:9<791::AID-ESP888>3.0.CO;2-X

Haun, S., Olsen, N. R. B., & Feurich, R. (2011). Numerical modeling of flow over trapezoidal broad-crested weir. *Engineering Applications of Computational Fluid Mechanics*, *5*(3), 397–405. https://doi.org/10.1080/19942060.2011.11015381

House, P. K., Webb, R. H., Baker, V. R., & Levish, D. R. (2002). *Ancient floods, modern hazards: Principles and applications of paleoflood hydrology* (Vol. 5). American Geophysical Union. https://doi.org/10.1029/WS005

Howard, A. D. (1994). A detachment-limited model of drainage basin evolution. *Water Resources Research*, *30*(7), 2261–2285. https://doi.org/10.1029/94WR00757

Hughes, S. A. (1993). *Physical models and laboratory techniques in coastal engineering* (Vol. 7). World Scientific. https://doi.org/10.1142/2154

Hungr, O., Leroueil, S., & Picarelli, L. (2014). The Varnes classification of landslide types, an update. *Landslides*, *11*(2), 167–194. https://doi.org/10.1007/s10346-013-0436-y

Iverson, R. M. (2012). Elementary theory of bed-sediment entrainment by debris flows and avalanches. *Journal of Geophysical Research*, *117*(F3), F03006. https://doi.org/10.1029/2011JF002189

Iverson, R. M. (2015). Scaling and design of landslide and debris-flow experiments. *Geomorphology*, *244*, 9–20. https://doi.org/10.1016/j.geomorph.2015.02.033

Izumi, N., & Parker, G. (2000). Linear stability analysis of channel inception: Downstream-driven theory. *Journal of Fluid Mechanics*, *419*, 239–262. https://doi.org/10.1017/S0022112000001427

Jiang, G.-S., Levy, D., Lin, C.-T., Osher, S., & Tadmor, E. (1998). High-resolution nonoscillatory central schemes with nonstaggered grids for hyperbolic conservation laws. *SIAM Journal on Numerical Analysis*, *35*(6), 2147–2168. https://doi.org/10.1137/S0036142997317560

Jiang, X. G., Wörman, A., Chen, P. S., Huang, Q., & Chen, H. Y. (2020). Mechanism of the progressive failure of non-cohesive natural dam slopes. *Geomorphology*, *363*, 107198. https://doi.org/10.1016/j.geomorph.2020.107198

Johnson, C. G., Kokelaar, B. P., Iverson, R. M., Logan, M., LaHusen, R. G., & Gray, J. M. N. T. (2012). Grain-size segregation and levee formation in geophysical mass flows. *Journal of Geophysical Research*, *117*(F1), F01032. https://doi.org/10.1029/2011JF002185

Johnson, J. P., & Whipple, K. X. (2010). Evaluating the controls of shear stress, sediment supply, alluvial cover, and channel morphology on experimental bedrock incision rate. *Journal of Geophysical Research*, *115*(F2), F02018. https://doi.org/10.1029/2009JF001335

Knapen, A., Poesen, J., Govers, G., Gyssels, G., & Nachtergaele, J. (2007). Resistance of soils to concentrated flow erosion: A review. *Earth-Science Reviews*, *80*(1–2), 75–109. https://doi.org/10.1016/j.earscirev.2006.08.001

Korup, O. (2002). Recent research on landslide dams-a literature review with special attention to New Zealand. *Progress in Physical Geography*, *26*(2), 206–235. https://doi.org/10.1191/0309133302pp333ra

Korup, O. (2004). Geomorphometric characteristics of New Zealand landslide dams. *Engineering Geology*, *73*(1–2), 13–35. https://doi.org/10.1016/j.enggeo.2003.11.003

Korup, O. (2005). Geomorphic hazard assessment of landslide dams in South Westland, New Zealand: Fundamental problems and approaches. *Geomorphology*, *66*(1–4), 167–188. https://doi.org/10.1016/j.geomorph.2004.09.013

Korup, O., & Tweed, F. (2007). Ice, moraine, and landslide dams in mountainous terrain. *Quaternary Science Reviews*, *26*(25–28), 3406–3422. https://doi.org/10.1016/j.quascirev.2007.10.012

Kurganov, A., & Tadmor, E. (2000). New high-resolution central schemes for nonlinear conservation laws and convection–diffusion equations. *Journal of Computational Physics*, *160*(1), 241–282. https://doi.org/10.1006/jcph.2000.6459

Lang, K. A., Huntington, K. W., & Montgomery, D. R. (2013). Erosion of the Tsangpo Gorge by megafloods, eastern Himalaya. *Geology*, *41*(9), 1003–1006. https://doi.org/10.1130/g34693.1

Larese, A., Rossi, R., Oñate, E., Toledo, M. Á., Morán, R., & Campos, H. (2015). Numerical and experimental study of overtopping and failure of rockfill dams. *International Journal of Geomechanics*, *15*(4), 04014060. https://doi.org/10.1061/(ASCE)GM.1943-5622.0000345

LaViolette, M. (2017). On the history, science, and technology included in the Moody diagram. *Journal of Fluids Engineering*, *139*(3), 030801. https://doi.org/10.1115/1.4035116

Macchione, F., & Rino, A. (2008). Model for predicting floods due to earthen dam breaching. II: Comparison with other methods and predictive use. *Journal of Hydraulic Engineering*, *134*(12), 1697–1707. https://doi.org/10.1061/(ASCE)0733-9429(2008)134:12(1697

Mitchell, J. K., & Soga, K. (2005). *Fundamentals of soil behavior* (Vol. 3). John Wiley & Sons.

Nessyahu, H., & Tadmor, E. (1990). Non-oscillatory central differencing for hyperbolic conservation laws. *Journal of Computational Physics*, *87*(2), 408–463. https://doi.org/10.1016/0021-9991(90)90260-8

Niu, Z.-P., Xu, W.-L., Li, N.-W., Xue, Y., & Chen, H.-Y. (2012). Experimental investigation of the failure of cascade landslide dams. *Journal of Hydrodynamics*, *24*(3), 430–441. https://doi.org/10.1016/s1001-6058(11)60264-3

21699011, 2022, 10, Downloaded from https://agupubs.onlinelibrary.wiley.com/doi/10.1029/2022JF006664 by Helmholtz-Zentrum Potsdam GFZ, Wiley Online Library on [21/11/2022]. See the Terms and Conditions (https://onlinelibrary.wiley.com/terms-and-conditions) on Wiley Online Library for rules of use; OA articles are governed by the applicable Creative Commons License

O'Connor, J., & Beebee, R. A. (2009). Floods from natural rock-material dams. *Megaflooding on Earth and Mars*, 128–171. https://doi.org/10.1017/CBO9780511635632.008

OriginPro. (2022). OriginPro v.2022b education edition [Software]. OriginLab Corporation. Retrieved from https://www.originlab.com/

Papa, M., Egashira, S., & Itoh, T. (2004). Critical conditions of bed sediment entrainment due to debris flow. *Natural Hazards and Earth System Sciences, Copernicus Publications on Behalf of the European Geosciences Union*, *4*(3), 469–474. Retrieved from https://hal.archives-ouvertes.fr/hal-00299152

Paphitis, D. (2001). Sediment movement under unidirectional flows: An assessment of empirical threshold curves. *Coastal Engineering*, *43*(3–4), 227–245. https://doi.org/10.1016/S0378-3839(01)00015-1

Parker, G., & Izumi, N. (2000). Purely erosional cyclic and solitary steps created by flow over a cohesive bed. *Journal of Fluid Mechanics*, *419*, 203–238. https://doi.org/10.1017/S0022112000001403

Partheniades, E. (1965). Erosion and deposition of cohesive soils. *Journal of the Hydraulics Division*, *91*(1), 105–139. https://doi.org/10.1061/JYCEAJ.0001165

Peng, M., Ma, C. Y., Chen, H. X., Zhang, P., Zhang, L. M., Jiang, M. Z., et al. (2021). Experimental study on breaching mechanisms of landslide dams composed of different materials under surge waves. *Engineering Geology*, *291*, 106242. https://doi.org/10.1016/j.enggeo.2021.106242

Peng, M., & Zhang, L. M. (2012). Breaching parameters of landslide dams. *Landslides*, *9*(1), 13–31. https://doi.org/10.1007/s10346-011-0271-y

Pontillo, M., Schmocker, L., Greco, M., & Hager, W. H. (2010). 1D numerical evaluation of dike erosion due to overtopping. *Journal of Hydraulic Research*, *48*(5), 573–582. https://doi.org/10.1080/00221686.2010.507005

Powledge, G. R., Ralston, D. C., Miller, P., Chen, Y. H., Clopper, P. E., & Temple, D. (1989). Mechanics of overflow erosion on embankments. II: Hydraulic and design considerations. *Journal of Hydraulic Engineering*, *115*(8), 1056–1075. https://doi.org/10.1061/(ASCE)0733-9429(1989)115:8(1056)

Rosgen, D. L. (1994). A classification of natural rivers. *Catena*, *22*(3), 169–199. https://doi.org/10.1016/0341-8162(94)90001-9

Ruan, H., Chen, H., Li, Y., Chen, J., & Li, H. (2021). Study on the downcutting rate of a debris flow dam based on grain-size distribution. *Geomorphology*, *391*, 107891. https://doi.org/10.1016/j.geomorph.2021.107891

Savage, S. B., & Hutter, K. (1989). The motion of a finite mass of granular material down a rough incline. *Journal of Fluid Mechanics*, *199*, 177–215. https://doi.org/10.1017/s0022112089000340

Schneider, C. A., Rasband, W. S., & Eliceiri, K. W. (2012). NIH image to ImageJ: 25 years of image analysis. *Nature Methods*, *9*(7), 671–675. https://doi.org/10.1038/nmeth.2089

Sheng, Y. P., & Lick, W. (1979). The transport and resuspension of sediments in a shallow lake. *Journal of Geophysical Research*, *84*(C4), 1809–1826. https://doi.org/10.1029/JC084iC04p01809

Singh, V. P., & Scarlatos, P. D. (1988). Analysis of gradual earth-dam failure. *Journal of Hydraulic Engineering*, *114*(1), 21–42. https://doi.org/10.1061/(ASCE)0733-9429(1988)114:1(21)

Sweby, P. K. (1984). High resolution schemes using flux limiters for hyperbolic conservation laws. *SIAM Journal on Numerical Analysis*, *21*(5), 995–1011. https://doi.org/10.1137/0721062

Szymkiewicz, R. (2010). *Numerical modeling in open channel hydraulics* (1 ed., Vol. 83). Springer Science & Business Media. https://doi.org/10.1007/978-90-481-3674-2

Takahashi, T. (1991). *Debris flow: Mechanics, prediction and countermeasures* (1st ed.). CRC Press/Balkema. https://doi.org/10.1201/9780203946282

Turowski, J. M., Badoux, A., & Rickenmann, D. (2011). Start and end of bedload transport in gravel-bed streams. *Geophysical Research Letters*, *38*(4), L04401. https://doi.org/10.1029/2010GL046558

Turowski, J. M., Lague, D., Crave, A., & Hovius, N. (2006). Experimental channel response to tectonic uplift. *Journal of Geophysical Research*, *111*(F3), F03008. https://doi.org/10.1029/2005JF000306

Turzewski, M. D., Huntington, K. W., & LeVeque, R. J. (2019). The geomorphic impact of outburst floods: Integrating observations and numerical simulations of the 2000 Yigong flood, eastern Himalaya. *Journal of Geophysical Research: Earth Surface*, *124*(5), 1056–1079. https://doi.org/10.1029/2018JF004778

Visser, P. J. (1999). Breach erosion in sand-dikes. *26th International Conference on Coastal Engineering*, 3516–3528. https://doi.org/10.1061/9780784404119.267

Wainwright, J., Parsons, A. J., Cooper, J. R., Gao, P., Gillies, J. A., Mao, L., et al. (2015). The concept of transport capacity in geomorphology. *Reviews of Geophysics*, *53*(4), 1155–1202. https://doi.org/10.1002/2014RG000474

Walder, J. S., Iverson, R. M., Godt, J. W., Logan, M., & Solovitz, S. A. (2015). Controls on the breach geometry and flood hydrograph during overtopping of noncohesive earthen dams. *Water Resources Research*, *51*(8), 6701–6724. https://doi.org/10.1002/2014WR016620

Walder, J. S., & O'Connor, J. E. (1997). Methods for predicting peak discharge of floods caused by failure of natural and constructed earthen dams. *Water Resources Research*, *33*(10), 2337–2348. https://doi.org/10.1029/97WR01616

Walsh, A., McDougall, S., Evans, S. G., & Take, W. A. (2021). Effect of upstream dam geometry on peak discharge during overtopping breach in noncohesive homogeneous embankment dams; implications for Tailings dams. *Water Resources Research*, *57*(12), e2020WR029358. https://doi.org/10.1029/2020wr029358

Wang, Z. Y. (1999). Experimental study on scour rate and river bed inertia. *Journal of Hydraulic Research*, *37*(1), 17–37. https://doi.org/10.1080/00221689909498530

Wu, W. M. (2013). Simplified physically based model of earthen embankment breaching. *Journal of Hydraulic Engineering*, *139*(8), 837–851. https://doi.org/10.1061/(ASCE)HY.1943-7900.0000741

Wu, W. M., Perera, C., Smith, J., & Sanchez, A. (2018). Critical shear stress for erosion of sand and mud mixtures. *Journal of Hydraulic Research*, *56*(1), 96–110. https://doi.org/10.1080/00221686.2017.1300195

Yang, F. G., Zhou, X. Q., Liu, X. N., Cao, S. Y., & Huang, E. (2011). Experimental study of breach growth processes in sand dams of quake lakes. *Journal of Earthquake Tsunami*, *5*(5), 445–459. https://doi.org/10.1142/S1793431111001182

Zhang, H. W. (2012). A unified formula for incipient velocity of sediment [In Chinese]. *Journal of Hydraulic Engineering*, *43*(12), 1387–1396. CNKI:SUN:SLXB.0.2012-12-003.

Zhang, J. Y., Fan, G., Li, H. B., Zhou, J. W., & Yang, X. G. (2021). Large-scale field model tests of landslide dam breaching. *Engineering Geology*, *293*, 106322. https://doi.org/10.1016/j.enggeo.2021.106322

Zhang, L. M., Peng, M., Chang, D. S., & Xu, Y. (2016). *Dam failure mechanisms and risk assessment*. John Wiley & Sons. https://doi.org/10.1002/9781118558522

Zhong, Q. M., Chen, S. S., Deng, Z., & Mei, S. A. (2019). Prediction of overtopping-induced breach process of cohesive dams. *Journal of Geotechnical and Geoenvironmental Engineering*, *145*(5), 04019012. https://doi.org/10.1061/(ASCE)GT.1943-5606.0002035

21699011, 2022, 10, Downloaded from https://agupubs.onlinelibrary.wiley.com/doi/10.1029/2022JF006664 by Helmholtz-Zentrum Potsdam GFZ, Wiley Online Library on [21/11/2022]. See the Terms and Conditions (https://onlinelibrary.wiley.com/terms-and-conditions) on Wiley Online Library for rules of use; OA articles are governed by the applicable Creative Commons License

Zhong, Q. M., Chen, S. S., Mei, S. A., & Cao, W. (2018). Numerical simulation of landslide dam breaching due to overtopping. *Landslides*, *15*(6), 1183–1192. https://doi.org/10.1007/s10346-017-0935-3

Zhou, G. G., Roque, P. J. C., Xie, Y., Song, D., Zou, Q., & Chen, H. (2020). Numerical study on the evolution process of a geohazards chain resulting from the Yigong landslide. *Landslides*, *17*(11), 2563–2576. https://doi.org/10.1007/s10346-020-01448-w

Zhou, G. G. D., Cui, P., Tang, J. B., Chen, H. Y., Zou, Q., & Sun, Q. C. (2015). Experimental study on the triggering mechanisms and kinematic properties of large debris flows in Wenjia Gully. *Engineering Geology*, *194*, 52–61. https://doi.org/10.1016/j.enggeo.2014.10.021

Zhou, G. G. D., Lu, X. Q., Xie, Y. X., Cui, K. F. E., & Tang, H. (2022). Mechanisms of the non-uniform breach channel evolution of landslide dams composed of unconsolidated sediments during overtopping failure [Dataset]. Zenodo. https://doi.org/10.5281/zenodo.7050542

Zhou, G. G. D., Zhou, M. J., Shrestha, M. S., Song, D. R., Choi, C. E., Cui, K. F. E., et al. (2019). Experimental investigation on the longitudinal evolution of landslide dam breaching and outburst floods. *Geomorphology*, *334*, 29–43. https://doi.org/10.1016/j.geomorph.2019.02.035

Zhou, M. J., Zhou, G. G. D., Cui, K. F. E., Song, D. R., & Lu, X. Q. (2019). Influence of inflow discharge and bed erodibility on outburst flood of landslide dam. *Journal of Mountain Science*, *16*(4), 778–792. https://doi.org/10.1007/s11629-018-5312-8

References From the Supporting Information

Amos, C., Bergamasco, A., Umgiesser, G., Cappucci, S., Cloutier, D., DeNat, L., et al. (2004). The stability of tidal flats in Venice Lagoon—The results of in-situ measurements using two benthic, annular flumes. *Journal of Marine Systems*, *51*(1–4), 211–241. https://doi.org/10.1016/j.jmarsys.2004.05.013

Cao, Z., Pender, G., Wallis, S., & Carling, P. (2004). Computational dam-break hydraulics over erodible sediment bed. *Journal of Hydraulic Engineering*, *130*(7), 689–703. https://doi.org/10.1061/(ASCE)0733-9429(2004)130:7(689)

Chiu, C. L. (1989). Velocity distribution in open channel flow. *Journal of Hydraulic Engineering*, *115*(5), 576–594. https://doi.org/10.1061/(ASCE)0733-9429(1989)115:5(576)

Cruff, R. (1965). *Cross-channel transfer of linear momentum in smooth rectangular channels*. US Government Printing Office. https://doi.org/10.3133/wsp1592B

Ghosh, S., & Roy, N. (1970). Boundary shear distribution in open channel flow. *Journal of the Hydraulics Division*, *96*(4), 967–994. https://doi.org/10.1061/JYCEAJ.0002477

Guo, J. K., & Julien, P. Y. (2005). Shear stress in smooth rectangular open-channel flows. *Journal of Hydraulic Engineering*, *131*(1), 30–37. https://doi.org/10.1061/(ASCE)0733-9429(2005)131:1(30)

Hanson, G., & Cook, K. (1997). Development of excess shear stress parameters for circular jet testing. *ASAE Paper, 972227*.

Julian, J. P., & Torres, R. (2006). Hydraulic erosion of cohesive riverbanks. *Geomorphology*, *76*(1–2), 193–206. https://doi.org/10.1016/j.geomorph.2005.11.003

Kartha, V. C., & Leutheusser, H. J. (1970). Distribution of tractive force in open channels. *Journal of the Hydraulics Division*, *96*(7), 1469–1483. https://doi.org/10.1061/JYCEAJ.0002562

Knight, D. W., Demetriou, J. D., & Hamed, M. E. (1984). Boundary shear in smooth rectangular channels. *Journal of Hydraulic Engineering*, *110*(4), 405–422. https://doi.org/10.1061/(ASCE)0733-9429(1984)110:4(405)

Lashkar-Ara, B., Fathi-Moghadam, M., Shafai-Bajestan, M., & Jael, A. (2010). Boundary shear stresses in smooth channels. *Journal of Food Agriculture and Environment*, *8*(1), 343–347. https://doi.org/10.1234/4.2010.1523

Lick, W., Jin, L., & Gailani, J. (2004). Initiation of movement of quartz particles. *Journal of Hydraulic Engineering*, *130*(8), 755–761. https://doi.org/10.1061/(ASCE)0733-9429(2004)130:8(755)

McDougall, S., & Hungr, O. (2005). Dynamic modelling of entrainment in rapid landslides. *Canadian Geotechnical Journal*, *42*(5), 1437–1448. https://doi.org/10.1139/t05-064

Mehta, A. (1988). Laboratory studies on cohesive sediment deposition and erosion. In *Physical processes in estuaries* (pp. 427–445). Springer. https://doi.org/10.1007/978-3-642-73691-3_21

Mitchener, H., & Torfs, H. (1996). Erosion of mud/sand mixtures. *Coastal Engineering*, *29*(1–2), 1–25. https://doi.org/10.1016/S0378-3839(96)00002-6

Myers, W. (1978). Momentum transfer in a compound channel. *Journal of Hydraulic Research*, *16*(2), 139–150. https://doi.org/10.1080/00221687809499626

Noutsopoulos, G. C., & Hadjipanos, P. (1982). Discussion: Boundary shear in smooth and rough channels. *Journal of the Hydraulics Division, Proceedings of the American Society of Civil Engineers*, *108*(6), 809–812. https://doi.org/10.1061/JYCEAJ.0005880

Ockenden, M., & Delo, E. (1988). Consolidation and erosion of estuarine mud and sand mixtures-an experimental study. HR Wallingford, Report No. SR 149.

Pickert, G., Weitbrecht, V., & Bieberstein, A. (2011). Breaching of overtopped river embankments controlled by apparent cohesion. *Journal of Hydraulic Research*, *49*(2), 143–156. https://doi.org/10.1080/00221686.2011.552468

Prasad, V. R. B. (1991). Velocity, shear and friction factor studies in rough rectangular open channels for super critical flow (PhD thesis). *Indian Institute of Science*.

Rifai, I., El Kadi Abderrezzak, K., Erpicum, S., Archambeau, P., Violeau, D., Pirotton, M., & Dewals, B. (2018). Floodplain backwater effect on overtopping induced fluvial dike failure. *Water Resources Research*, *54*(11), 9060–9073. https://doi.org/10.1029/2017WR022492

Rifai, I., Erpicum, S., Archambeau, P., Violeau, D., Pirotton, M., El Kadi Abderrezzak, K., & Dewals, B. (2017). Overtopping induced failure of noncohesive, homogeneous fluvial dikes. *Water Resources Research*, *53*(4), 3373–3386. https://doi.org/10.1002/2016WR020053

Roberts, J., Jepsen, R., Gotthard, D., & Lick, W. (1998). Effects of particle size and bulk density on erosion of quartz particles. *Journal of Hydraulic Engineering*, *124*(12), 1261–1267. https://doi.org/10.1061/(ASCE)0733-9429(1998)124:12(1261)

Seckin, G., Seckin, N., & Yurtal, R. (2006). Boundary shear stress analysis in smooth rectangular channels. *Canadian Journal of Civil Engineering*, *33*(3), 336–342. https://doi.org/10.1139/l05-110

Shen, G. Z., Sheng, J. B., Xiang, Y., Zhong, Q. M., & Yang, D. W. (2020). Numerical modeling of overtopping-induced breach of landslide dams. *Natural Hazards Review*, *21*(2), 04020002. https://doi.org/10.1061/(ASCE)NH.1527-6996.0000362

Smerdon, E. T., & Beasley, R. P. (1961). Critical tractive forces in cohesive soils. *Agricultural Engineering*, *42*(1), 26–29.

Vanoni, V. A. (1964). Measurements of critical shear stress for entraining fine sediments in a boundary layer. In *W. M. Keck Laboratory of Hydraulics and Water Resources Report, 7. California Institute of Technology, Pasadena, CA*. Retrieved from https://resolver.caltech.edu/CaltechKHR:KH-R-7

Yang, S. Q., & Lim, S. Y. (1997). Mechanism of energy transportation and turbulent flow in a 3D channel. *Journal of Hydraulic Engineering*, *123*(8), 684–692. https://doi.org/10.1061/(ASCE)0733-9429(1997)123:8(684)

21699011, 2022, 10, Downloaded from https://agupubs.onlinelibrary.wiley.com/doi/10.1029/2022JF006664 by Helmholtz-Zentrum Potsdam GFZ, Wiley Online Library on [21/11/2022]. See the Terms and Conditions (https://onlinelibrary.wiley.com/terms-and-conditions) on Wiley Online Library for rules of use; OA articles are governed by the applicable Creative Commons License

Yang, S. Q., & Lim, S. Y. (1998). Boundary shear stress distributions in smooth rectangular open channel flows. *ICE Proceedings Water Maritime and Energy*, *130*(3), 163–173. https://doi.org/10.1680/iwtme.1998.30975

Yang, S. Q., & Lim, S. Y. (2002). A geometrical method for computing the distribution of boundary shear stress across irregular straight open channels: By SR KHODASHENAS and A. PAQUIER. *Journal of Hydraulic Research*, *37*(3), 381–388. https://doi.org/10.1080/00221680209499896

Zarrati, A., Jin, Y. C., & Karimpour, S. (2008). Semianalytical model for shear stress distribution in simple and compound open channels. *Journal of Hydraulic Engineering*, *134*(2), 205–215. https://doi.org/10.1061/(ASCE)0733-9429(2008)134:2(205)

Zhang, L. M., Xiao, T., He, J., & Chen, C. (2019). Erosion-based analysis of breaching of Baige landslide dams on the Jinsha River, China, in 2018. *Landslides*, *16*(10), 1965–1979. https://doi.org/10.1007/s10346-019-01247-y

21699011, 2022, 10, Downloaded from https://agupubs.onlinelibrary.wiley.com/doi/10.1029/2022JF006664 by Helmholtz-Zentrum Potsdam GFZ, Wiley Online Library on [21/11/2022]. See the Terms and Conditions (https://onlinelibrary.wiley.com/terms-and-conditions) on Wiley Online Library for rules of use; OA articles are governed by the applicable Creative Commons License